LABORATORI NAZIONALI DI FRASCATI
SIS – Pubblicazioni

LNF-94/077 (P)
22 Dicembre 1994

Status of DAΦNE and KLOE

Juliet Lee-Franzini

INFN – Laboratori Nazionali di Frascati, P.O. Box 13, I-Frascati (Roma) Italy, and
Physics Department, SUNY at Stony Brook, New York 11794, USA

Abstract

An e^+e^- collider, christened DAΦNE, optimized for operation at a total energy of 1020 MeV, the mass of the ϕ meson, is now under construction at the Laboratori Nazionali di Frascati of the INFN. Here we report on DAΦNE's machine parameters, ϕ production rates and its present status. We discuss its particle physics program, which includes CP violation and other symmetry studies, tests of chiral pertubation calculations and light meson spectroscopy. The general purpose detector, KLOE, being built for performing these experiments is described and its current progress is discussed.

PACS.: 11.30.Er; 13.20.Jf; 29.40.Gx; 29.40.Vj

Contribution to the "Second DAΦNE Physics Handbook"

TABLE OF CONTENTS

1. DAΦNE

In June 1990 the first high luminosity e^+e^- colliders was approved and funded by the Istituto Nazionale di Fisica Nucleare, INFN, of Italy. It is an e^+e^- collider optimized for operation at a total energy of 1020 MeV, the mass of the ϕ meson. The machine, a so called ϕ-factory, has been christened DAΦNE, for Double Anular Φ-factory for Nice Experiments.[1] DAΦNE consists of two coplanar rings, a linac and an accumulator for fast topping-off. All components to be installed in the buildings which housed the ADONE collider. The machine complex of DAΦNE is shown in Fig. 1.

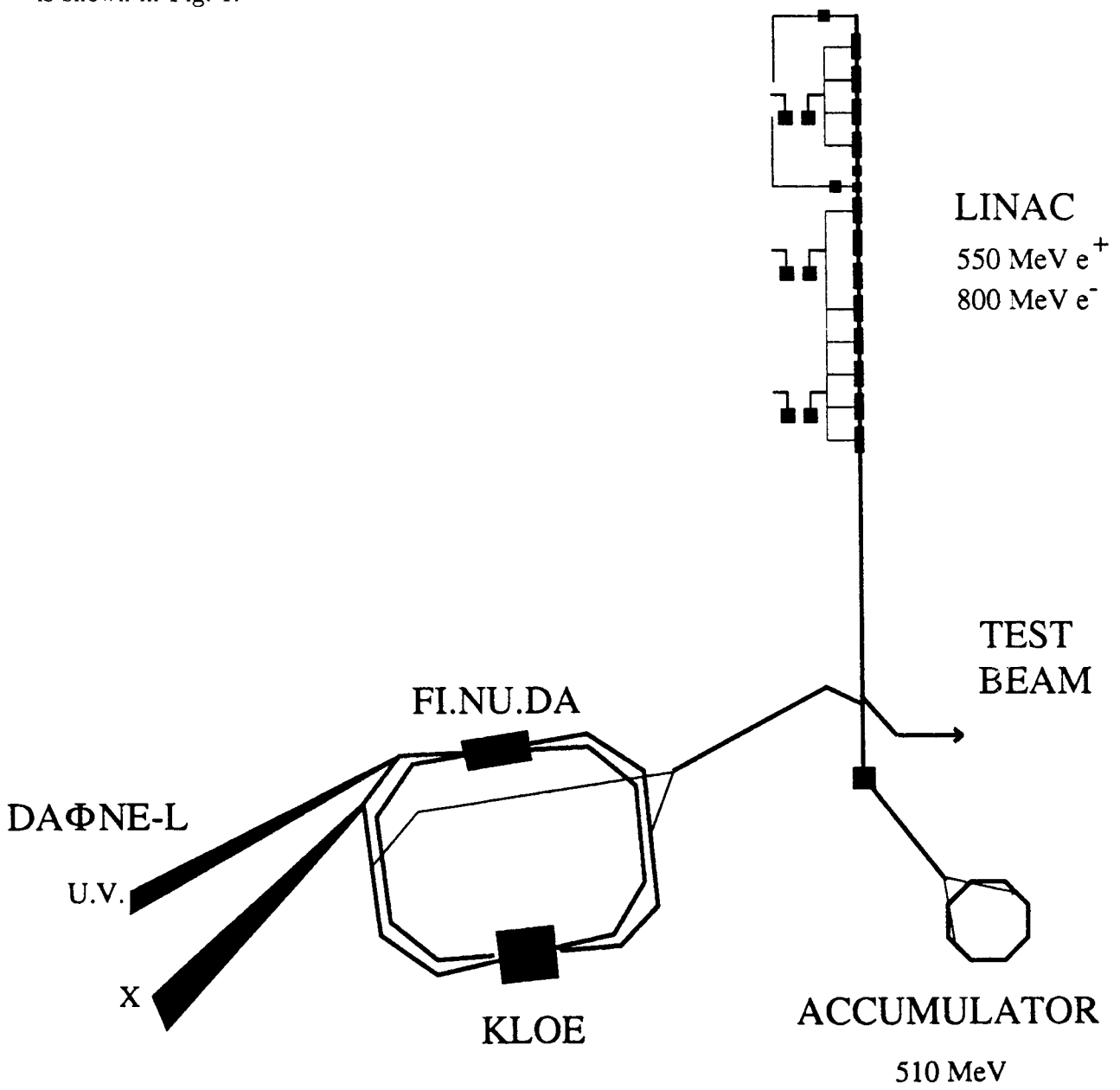

Fig. 1. The DAΦNE machine complex.

There will be two interaction areas, for the two experiments KLOE (particle physics) and FINUDA (nuclear physics). There is as well the possibility for other research with the ultraviolet and x-ray beams of the DAΦNE-L(ight) facility. The DAΦNE beam energy will be 0.51 GeV with an *rms* energy spread of 0.4 MeV, the same as the injection energy, which means there will be no energy ramping in the rings in the normal running mode at the ϕ resonance. The $e^{\pm}$ are accelerated in the *linac*, a linear accelerator consisting of two pieces, one that imparts a maximum of 250 MeV, the other 550 MeV. The electrons thus could in principle be accelerated to a maximum of 800 MeV. The positrons are created at the end of the first segment and accelerated in the second. The beams are then stored and "cooled" to reduce the momentum spread in the small accumulator ring, before injection into the main rings. The magnetic element layout of the DAΦNE rings are shown in Fig. 2.

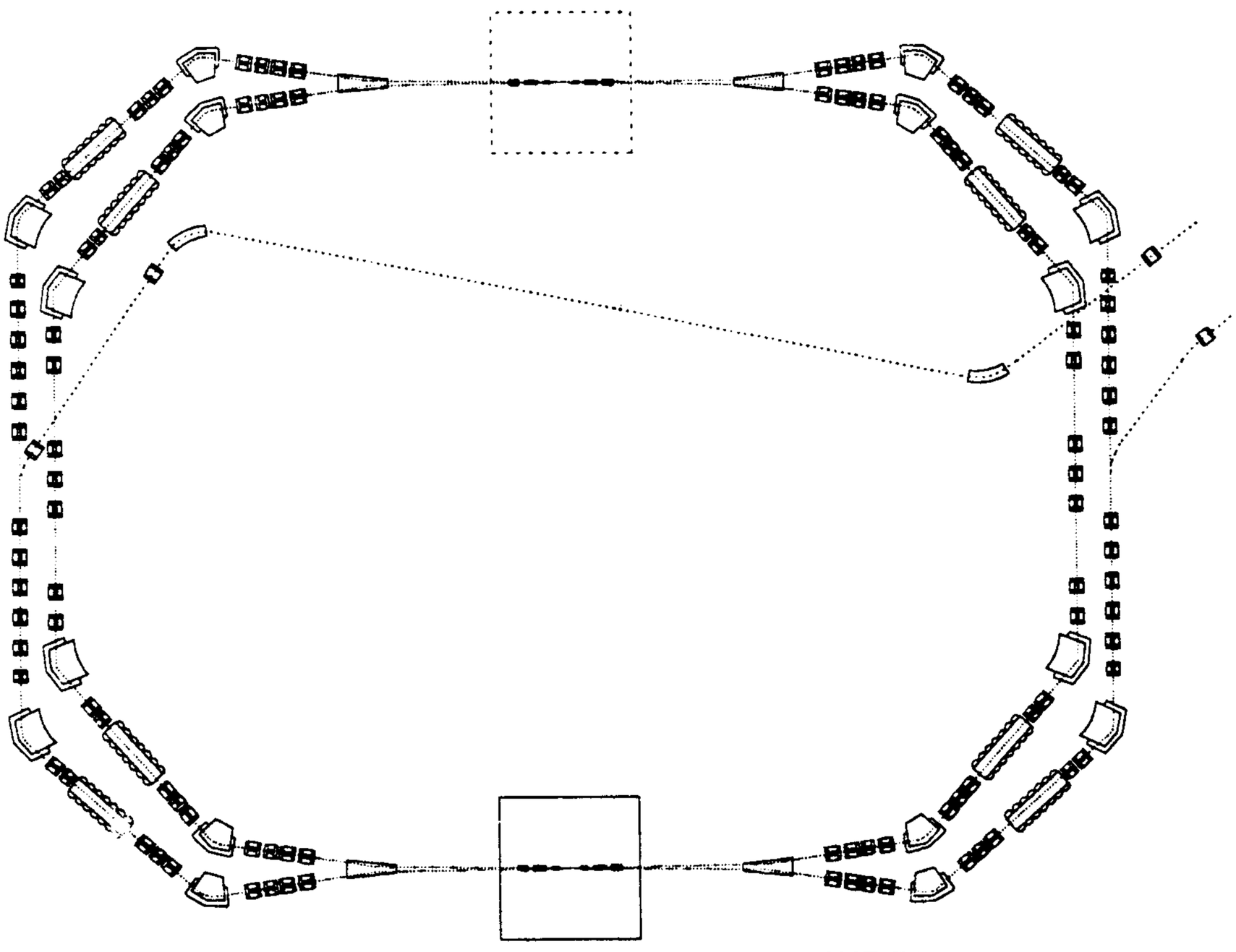

Fig. 2. Magnetic Layout of the DAΦNE Rings .

The operating energy range is up to 1.5 GeV. The initial luminosity is expected to be $\sim 10^{32}$ $cm^{-2}\,s^{-1}$. The final target luminosity is $\mathcal{L}\sim 10^{33}\ cm^{-2}\,s^{-1}$. Both values apply at the ϕ peak. The ring size allows for operation with up to 120 bunches in each ring, filling every RF bucket, at the operating frequency of 370 MHz. An estimate of the DAΦNE luminosity is obtained by scaling from the VEPP–2M collider, operating at Novosibirsk, with *flat* beams and two interactions per turn, at the ϕ peak. The single bunch luminosity for DAΦNE is $\mathcal{L}_0 = 7.2\times 10^{30}\ cm^{-2}\,s^{-1}$ and for 120 bunches $\mathcal{L}\sim 9\times 10^{32}\ cm^{-2}\,s^{-1}$. The final expected luminosity can therefore be obtained with a conservative single bunch value, paying however in a very large value of the circulating currents, ~5 A.

The DAΦNE lattice is a four-period modified Chasman-Green type, with each achromat

incorporating a two meter long wiggler to lower the beam damping time. All paramaters of the machine are tunable through independent control of all elements, in order to maximize $\mathcal{L}_0$ and properly cure multibunch instabilities. The low-β insertion is a compromise between machine choices and experimental requirements. The free distance between the innermost quadrupoles is 80 cm and the insertion occults a cone of 9° half opening. Rare earths-cobalt permanent magnet quadrupoles are used. The DAΦNE machine parameters are listed below.

1.1 Parameters

Table 1. DAΦNE machine parameters

Commissioning Date	1966
Beam Energy	0.510 GeV
Luminosity	$(1.35 \rightarrow 5.40) \times 10^{32}$
Time between collisions	10.8→2.7 ns
Crossing half-angle	10 to 15 mrad
Energy spread	0.4×10^{-3}, rms
Bunch length	3.0 cm
Beam size at IR	2.1 mm horizontal 21 μm vertical
Free space at interaction point	±0.46 m
Luminosity lifetime	3.0 hours
Topping up time	< 2′
Injection Energy	0.510 GeV
Transverse emittance	$1000 \times \pi \cdot 10^{-9}$ mrad, hor. $10 \times \pi \cdot 10^{-9}$ mrad, vert.
β^*	4.5 m, horizontal 4.5 cm, vertical
Beam-beam tune shift/crossing	0.04
RF Frequency	368.25 MHz
Particles/bunch	8.9×10^{10}
Bunches per ring e^+ and e^-	30→120
Average beam current e^+ and e^-	1313→5250 mA
Orbit length	97.7 m
Interaction Regions	2
Utility insertions	2×2
Magnetic length of dipoles	1.21, 0.99 m
Dipoles in ring	8 (+4 wigglers)
Quadrupoles in ring	51
Peak magnetic field	Dipoles: 1.2→1.76 T Wigglers: 1.8 T

1.2 ϕ-PRODUCTION

At the target luminosity of DAΦNE and given that the cross section for $e^+e^- \rightarrow \phi$ at the ϕ resonance peak is $\sim 5\mu$b, some 5000 ϕ's are produced per second. Adopting the canonical definition in high energy physics of one calendar year equals 10^7 seconds, which generously takes into account the various integrated luminosity degradation factors, such as peak versus average luminosity, loss due to machine study and maintenance periods, and possible detector down times, the production rate for ϕ's is still $\sim 5 \times 10^{10}$ per year!

The vector meson ϕ, whose quantum numbers are $J^{PC} = 1^{--}$, with mass $M = 1019.412 \pm 0.008$ MeV, total width $\Gamma = 4.41$ MeV and leptonic width $\Gamma_{ee} = 1.37$ keV, decays into other mesons with branching ratios, BR, as given in table 2 ![2] Included therein are also some relevant kinematical quantities, as well as the number of particles produced per year.

Table 2. ϕ decays.

Mode	BR %	β_K	$\gamma\beta c\tau]_K$ cm	p_{max} MeV/c	#/year
K^+K^-	49	0.249	95.4	127	2.5×10^{10} pairs
K_S	34	0.216	0.59	110	1.7×10^{10}
K_L	34	0.216	343.8	110	1.7×10^{10}
$\rho\pi$	13	–	–	182	6×10^9
$\pi^+\pi^-\pi^0$	2	–	–	462	1×10^9
$\eta\gamma$	1.3	–	–	362	6×10^8
other	~ 1	–	–	–	5×10^8

One notes therefore that DAΦNE is indeed a "factory" of neutral K's which are in a well prepared quantum state, of charged K pairs, as well as of ρ's, η's and the rarer η''s. The high luminosity of DAΦNE will also allow measurements of rare ϕ radiative decays. Another feature at DAΦNE is that, because the ϕ's decay at rest, kaons are produced in collinear pairs. The observation of one K guarantees the existence of the other, with determined direction and identity, *i.e.*, K's can be "tagged". Assuming a detector of a reasonable size, a very large numbers of tagged K mesons can be collected per year, as shown in table 3. The numbers are based on KLOE, the "general purpose detector" for DAΦNE,[3] [4] which is approximately 4 m in diameter and 4 m long, with a magnetic field B=6 kG, a K_S decay fiducial volume of radius $\sim$10 cm, and a K_L decay fiducial volume of radius 30 to 175 cm. This availability of tagged kaons is central to DAΦNE's ability for performing experiments not possible elsewhere, and enables KLOE to be essentially a "self-calibrating" via numerous K decay channels and Bhabha scattering. An absolute normalization of the K_S, K_L fluxes is also available.

Table 3. Tagged K meson decays

Mode	Tagged decays§
K_S	4.5×10^9
K_L	3.6×10^9
K^+ or K^-	1.7×10^{10}†
K^+ or K^-	3.4×10^9‡

§Detector efficiencies are approximately included.

†Using all $K^\pm$ decays, a good tag.

‡Using only $K^\pm \to \pi^0\pi^\pm$ decays, for a precision tag.

2. PHYSICS PROGRAM FOR A GENERAL DETECTOR AT DAΦNE

2.1 CP AND CPT AT DAΦNE BY QUANTUM INTERFEROMETRY

Consider the process $\phi \to KK \to f_1, t_1 + f_2, t_2$ where a K^0 meson decays into a state f_1 at time t_1 and the other into a state f_2 at time t_2, as illustrated below.

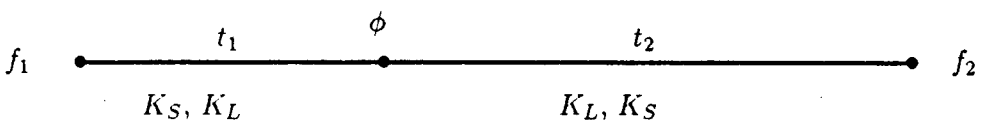

The decay intensity to f_1, f_2, as a function of $\Delta t = t_1 - t_2$ and for $\Delta t > 0$, is:

$$I(f_1,\ f_2;\ \Delta t) =$$
$$\frac{1}{2\Gamma}|\langle f_1|\ K_S\rangle\langle f_2|\ K_S\rangle|^2\Big(|\eta_1|^2 e^{-\Gamma_L \Delta t} + |\eta_2|^2 e^{-\Gamma_S \Delta t}$$
$$- 2|\eta_1||\eta_2| e^{-\Gamma \Delta t/2}\cos(\Delta m \Delta t + \phi_1 - \phi_2)\Big)$$

where $\eta_i = < f_i/K_L > / < f_i/K_S >$ and a similar expression holds for $\Delta t < 0$. The interference term is sensitive to Δm, the magnitude of the amplitude ratios η's and their phase difference, while the complete distribution depends also on the K_S and K_L lifetimes. One can thus perform a whole spectrum of precision "kaon-interferometry" experiments at DAΦNE by measuring the above decay intensity distributions by appropriate choice of the final states f_1, f_2. Four examples are listed below.

1. With $f_1 = f_2$ one measures Γ_S, Γ_L and Δm, since all phases cancel. Rates can be measured to $\times 10$ improvement in accuracy and Δm to $\times 2$.
2. With $f_1 = \pi^+\pi^-$, $f_2 = \pi^0\pi^0$, one measures $\Re(\epsilon'/\epsilon)$ at large time differences, and $\Im(\epsilon'/\epsilon)$ for $|\Delta t| \leq 5\tau_s$. Fig. 3 shows the interference pattern for this case.
3. With $f_1 = \pi^+\ell^-\nu$ and $f_2 = \pi^-\ell^+\nu$, one can measure the CPT–violation parameter δ_K:[5] its real part at large time differences and the imaginary part for $|\Delta t| \leq 10\tau_s$. Fig. 4 shows the interference pattern.
4. For $f_1 = 2\pi$, $f_2 = K_{\ell 3}$, small time differences yield Δm, $|\eta_{\pi\pi}|$ and $\phi_{\pi\pi}$, while at large time differences, the asymmetry in K_L semileptonic decays provides tests of T and CPT. The *vacuum regeneration* interference is shown in fig. 5.

In all, by choosing appropriate f_1 and f_2 channels one can determine 16 independent parameters describing the neutral K system. If the validity of the $\Delta S = \Delta Q$ rule is assumed there are only 13 parameters to be determined. Experiments at DAΦNE can thus test CPT invariance, in addition to studying CP violation. Should however the $\Delta S = \Delta Q$ rule not hold (it is expected to be violated to only one part in 10^7 in the Standard Model), there are in fact 17 independent parameters.[6] Therefore we will need to use strangeness tagged K^0, which can be obtained from charge exchange of K^+ mesons, in turn tagged by observation of a K^- meson from the copious decay $\phi \to K^\pm$.

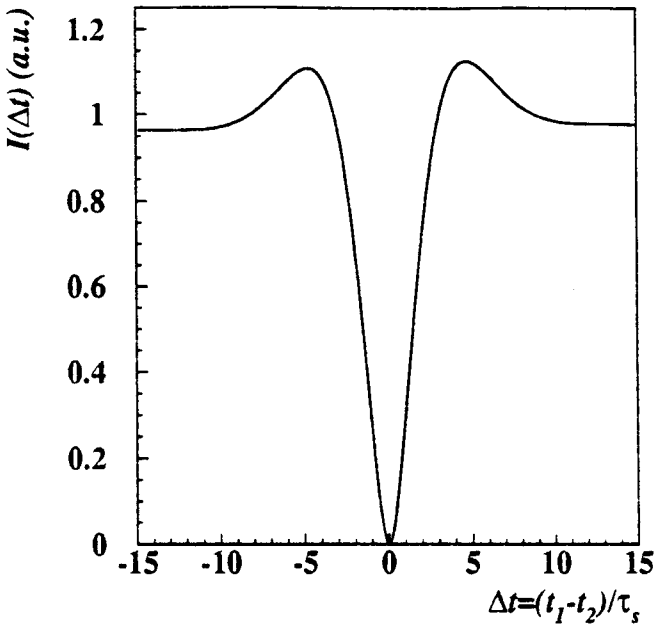

Fig. 3. Interference pattern for $f_1=\pi^+\pi^-$, $f_2=\pi^0\pi^0$

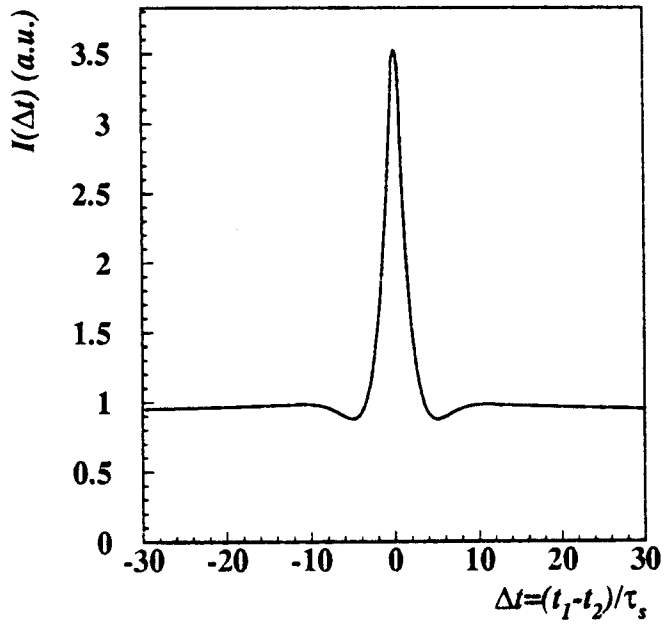

Fig. 4. Interference pattern for $f_1 = \ell^+$, $f_2 = \ell^-$

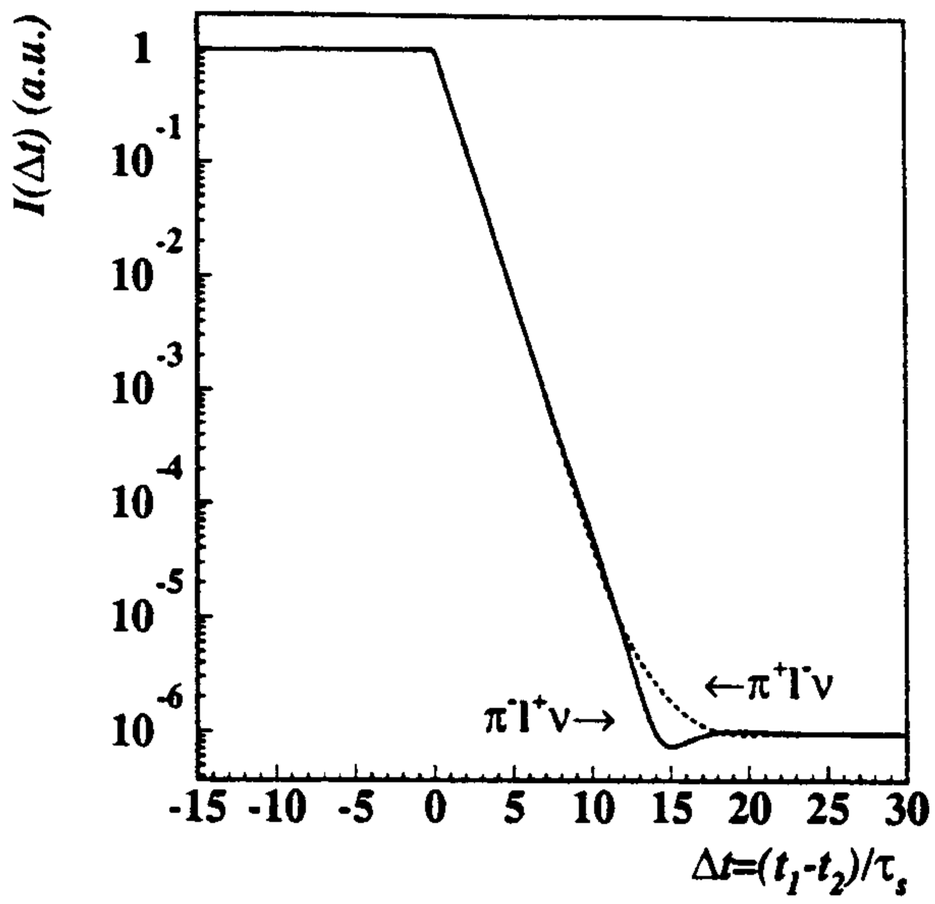

Fig. 5. Interference patten for $f_1 = \ell^{\pm}$, $f_2 = 2\pi$

2.2 Measuring $\mathcal{R}^{\pm}/\mathcal{R}^0$

We can also use the classical method of the double ratio $\mathcal{R}^{\pm}/\mathcal{R}^0 = 1+6\times\Re(\epsilon'/\epsilon)$, and other ways of measuring $\Re(\epsilon'/\epsilon)$ from selected final states. Very different systematics are involved, thus allowing a self check of the results. In fact, one can illustrate the statistical accuracy achievable at DAΦNE easily using the double ratio method (recall that the tagging efficiency drops out identically here and thus do not contribute to systematic errors).

In abbreviated form, the double ratio is

$$\mathcal{R}^{\pm}/\mathcal{R}^0 \;=\; \frac{N_L^{\pm}/N_S^{\pm}}{N_L^0/N_S^0} \approx 1 + 6\mathrm{Re}\frac{\epsilon'}{\epsilon}, \tag{2.1}$$

where each N refers to the number of $K_{L,S}$ decaying to two charged or neutral pions. The N_S numbers will evidently be much larger then the N_L; thus, the statistical errors coming from them will be negligible compared to those coming from the N_L. We thus have

$$\delta\left(\frac{\epsilon'}{\epsilon}\right) = \frac{1}{6}\sqrt{(\Delta N_L^{\pm})^2 + (\Delta N_L^0)^2} = \frac{1}{6}\sqrt{\frac{1}{N_L^{\pm}} + \frac{1}{N_L^0}} = \frac{1}{6}\sqrt{\frac{3}{2N_L^0}}, \tag{2.2}$$

since by isospin symmetry there are twice as many charged two pion decays as neutral two pion decays. N_L^0 is given by the ϕ cross-section, times the integrated luminosity per year, times the efficiency for K_L tags, times $BR(\phi \to K_L K_S)$, times $BR(K_L \to \pi^0\pi^0)$, times the number of K_L's that are within the fiducial volume (i.e., that are detectable):

$$N_L^0 = 5\ \mu\mathrm{b} \times 10^{10}\ \mu\mathrm{b}^{-1} \times 2/3 \times 0.34 \times 10^{-3} \times (1 - e^{-150/350}) = 4 \times 10^6, \tag{2.3}$$

which gives as claimed,

$$\delta\left(\frac{\epsilon'}{\epsilon}\right) = 1 \times 10^{-4}. \tag{2.4}$$

2.3 Other CP Violations at DAΦNE

So far CP violation has only been seen in K_L decays ($K_L \to \pi\pi$ and semileptonic decays). DAΦNE can look for $K_S \to \pi^0\pi^0\pi^0$, the counterpart to $K_L \to \pi\pi$. The branching ratio for this process is proportional to $\epsilon + \epsilon'_{000}$ where ϵ'_{000} is a quantity similar to ϵ', signalling direct CP violation. It is not as suppressed as the normal ϵ', perhaps a factor of twenty less. Nonetheless, as the expected BR is 2×10^{-9}, the whole signal will be at the 30 event level, and therefore there is here only the possibility to see the CP impurity of K_S, never observed before, not direct CP violation. The current limit on this BR is 3.7×10^{-5}. Another possibility is to look at the difference in rates between $K_S \to \pi^+ l^- \nu$ and $K_S \to \pi^- l^+ \nu$, which is expected to be $\sim 16 \times 10^{-4}$, not measurable in one year's running at DAΦNE, to an accuracy of $\sim 4 \times 10^{-4}$. Again this would be only a measurement of ϵ, not ϵ', but the observation for the first time of CP violation in two new channels of K_S decay would be nonetheless of considerable interest.

Evidence for direct CP violation can be also be obtained from the decays of charged kaons which are copiously produced at DAΦNE. CP requires equality of the partial rates for $K^\pm \to \pi^\pm\pi^+\pi^-$ ($\tau^\pm$) and for $K^\pm \to \pi^\pm\pi^0\pi^0$ ($\tau'^\pm$). One can improve the present rate asymmetry by two orders of magnitude. One can also observe differences in the Dalitz plot distributions for K^+ and K^- decays in both the τ and τ' modes; at DAΦNE one could reach sensitivities of $\sim 10^{-4}$. Finally, differences in rates in the radiative two pion decays of $K^\pm$, $K^\pm \to \pi^\pm\pi^0\gamma$, are also proof of direct CP violation. At DAΦNE the sensitivity reachable is $\sim 1.4 \times 10^{-3}$.

2.4 Chiral Perturbation Theory

In the last decade chiral perturbation theory (CHPT) has been extended to the next order terms in the chiral expansion ($\mathcal{O}(m^4)$, $\mathcal{O}(p^4)$, $\mathcal{O}(m^2p^2)$). Many new amplitudes can then be predicted.[7] At lowest order the CHPT relation predicts the slope of the scalar form factor, λ_0. There is at present disagreement from experiment with the CHPT prediction, 0.017 ± 0.004. one can measure λ_0 for K_L to an accuracy of 1.4×10^{-5}. Similar accuracy are obtainable for $K^\pm$ and for λ_+.

There is only one measurement of the relevant $K_{\ell 4}$ form factors. These decays provide an unique opportunity for the determination of the $\pi\pi$ phase shifts. This is discussed in detail in another section of this Handbook.[8]

The amplitudes for $K_{\ell 2,\gamma}$, $K_{\ell 2,e^+e^-}$ and $K_{\ell 3,\gamma}$ depend on the K charge radius. The rate for $K^\pm \to \pi^\pm\gamma\gamma$ and the $\gamma\gamma$ distributions are uniquely predicted by the chiral lagrangian approach. Dalitz decays of K mesons and two photon production of pions are also of great interest. At DAΦNE one can improve vastly on all these topics.

2.5 Radiative ϕ Decays

Many other physics topics can be studied, especially at the DAΦNE start up time, when the number of beam bunches will be approximately a quarter (30) of the final design value. An example is the study of light meson spectroscopy. Another is the study of rare radiative decays.

<u>$\phi \to \eta'\gamma$</u>

Precise measurements of the $\eta - \eta'$ mixing has important bearings on quark models and QCD, in particular on the question of whether there are gluonic components in the η and η'

wave functions.[9] In this regard, measurements of the radiative ϕ decays to η and to η', which are feasible with great sensitivity with KLOE, can lead to a really decisive test, when combined with the information coming from other sources such as the analogous J/Ψ decays and the two-photon decays of η and η'. To complete the determination of the η' parameters we need measurements of the rare transition $\phi \to \eta'\gamma$. There is some room for a non-vanishing gluonic component in the η'. To give an idea of the expected order of magnitude of the branching ratio, for no gluonium in the η' and a mixing angle of 20° we expect BR($\phi \to \eta'\gamma$)$\sim 1.2\times10^{-4}$. A Monte Carlo study[10] shows that KLOE can reach, during the commissioning year of DAΦNE, BR's of $\sim 10^{-6}$. This is another interesting piece of physics for KLOE in the context of quark models and QCD.

$\underline{\phi \to f_0\gamma}$

At the end of 1996, DAΦNE will begin delivering of the order of 500 ϕ -mesons/sec. This provides a unique opportunity to study the $f_0(975)$ in ϕ radiative decays, even for branching ratios which in some estimates could be as low as 1×10^{-6}. The unique, lightest scalar meson state $f_0(975)$ is poorly described by current models.[11] By Monte Carlo studies we show that the branching ratio above can easily be measured in the neutral decay channel $f_0 \to \pi^0\pi^0$.[12] In decays to $\pi^+\pi^-$, there are backgrounds from continuum processes.[13] Interference between one of these processes and the f_0 amplitude leads to very interesting and complex patterns.[14] A complete study of the photon spectrum from $e^+e^- \to \pi^+\pi^-\gamma$ at the ϕ peak, after suppression of continuum contributions by suitable kinematics and angular cuts, can determine the sign of the $\phi f_0\gamma$ coupling even for the smallest branching ratio, thus providing a totally new piece of information for the investigation of the nature of the f_0.[12]

2.6 The Strange Sea in the Nucleon

A study of KN interactions at low energies will shed light on the strange sea quark content in the nucleon.[15] Strange sea quark pairs seem to contribute to the static properties of the nucleon. to its mass, spin and magnetic moment. At present the low energy KN data base is extremely poor or even not existing. At DAΦNE the complex $K^{\pm}N$ scattering amplitudes at kinetic energies below $T_K = 14$ MeV can be studied for the first time. Neither the regeneration $K_L \to K_S$ cross section nor the elastic $K^{\pm}d$ scattering cross sections are known at present, Both would yield information on $K^{\pm}n$ scattering.

2.7 e^+e^- Annihilations into Hadrons from Threshold to 1.5 GeV

Precise measurements of $\sigma(e^+e^- \to \text{hadrons})$ up to energies of $\sim$1.5 GeV are necessary for the calculation of the muon anomaly a_μ.[16] The hadronic contributions to a_μ due to vacuum polarization and light by light scattering result in the largest uncertainty in a_μ. The estimate, based on poorly known cross sections for hadronic e^+e^- annihilation from the 2 pion threshold up to $\sim$ 1 GeV, gives:[16] $a_\mu^{hadr} = 702\,(19) \times 10^{-10}$; making it impossible to observe the weak interaction contribution which, to one loop, is[17] $a_\mu^{weak} = 19.5\,(0.1) \times 10^{-10}$. The required accuracy for the measurements[18] of $\sigma(e^+e^- \to \text{hadrons})$ is $\sim$ 0.5%, readily accessible to KLOE. This is discussed in detail elsewhere in this Handbook.

We recall that an accurate determination of the K form factor at the ϕ mass will allow measurements of the interference of the ϕ meson with the ρ, ω mesons and possibly with higher $s\bar{s}$ excitations. Finally spectroscopic studies up to 1.5 GeV are still of interest, for example, the search for the mysterious 1.1 GeV resonance.[19]

2.8 Conclusions

Aside from being an excellent, dedicated environment for studying CP violation, where ϵ'/ϵ will be determined to an accuracy of 10^{-4} in one year's running and *all* the K system parameters will be determined via interferometry, DAΦNE will also be a rich source of many other physics results. DAΦNE will for example be a unique source of pure K_S, thanks to tagging, providing up to 10^{10} kaons per year, and allowing measurements of rare K_S decay modes, most of which have not been measured yet, down to the 10^{-8} or 10^{-9} level. Rare charged K decay modes will also be studied. It will be a place to study many rare decays, such as $\phi \to \eta\gamma$, and η decays. In table 4 some of the improvements that may be made in various rare decay BR limits are listed.

Table 4. Rare decays at DAΦNE.

Decay mode	To date	Limits that can be achieved at DAΦNE
$\eta \to 3\gamma$	BR $< 5 \times 10^{-4}$	1.4×10^{-8}
$\eta \to \omega\gamma$	BR $< 5 \times 10^{-2}$	10^{-9}
$\phi \to \rho\gamma$	BR $< 2 \times 10^{-2}$	10^{-9}
$\phi \to \pi^+\pi^-\gamma$	BR $< 7 \times 10^{-3}$	10^{-9}
$\eta \to \pi^0 e^+ e^-$	BR $< 4 \times 10^{-5}$	1.4×10^{-8}
$\eta \to \pi^0 \mu^+ \mu^-$	BR $< 5 \times 10^{-6}$	1.4×10^{-8}

3. THE KLOE DESIGN

3.1 The KLOE LOGO

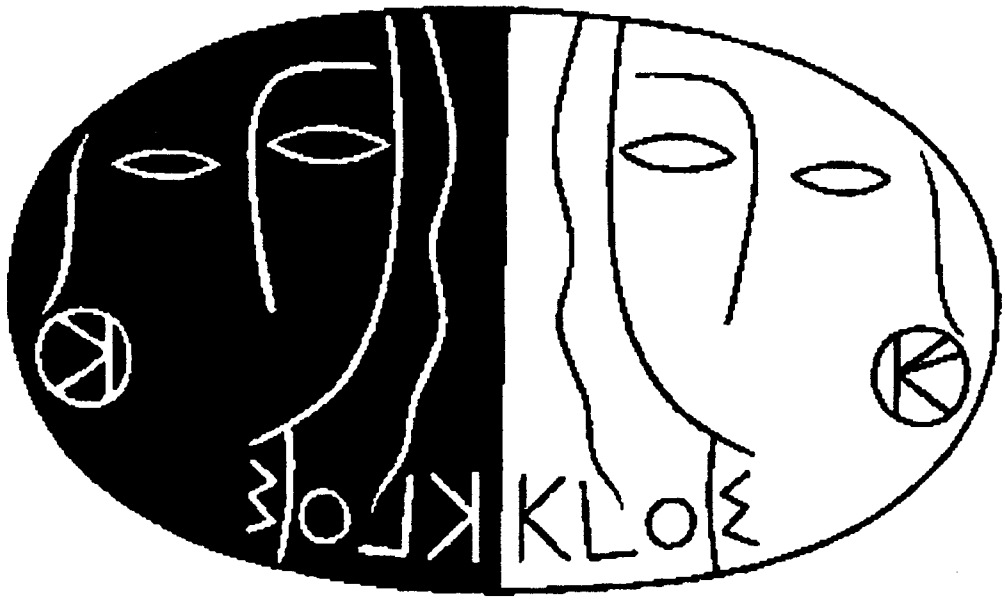

Fig. 6. KLOE LOGO.

3.2 Introduction

The KLOE-Detector, with its distinctive logo, was proposed to the LNF's Scientific committee and given stage-I approval April 28th, 1992.[3] A technical design proposal was submitted to the same committee on January 12th, 1993.[4] It was fully approved on March 19th, 1993. Two additional addenda were written to amplify design concerns specific to the central drift chamber,[20] and to the data acquisition system.[21] These four documents by the KLOE Collaboration are the source materials containing the full evolutionary details of the KLOE design. Here, I have extracted the salient features and parameters of the main components of the final detector and will mention some of the interesting results obtained during our prototyping and test work, to give a flavor of how much has been achieved and what still remains to be done.

The KLOE detector[3,4] is designed primarily with the goal of detecting direct CP violation in K^0 decays with a sensitivity of $\sim 10^{-4}$ in $\mathrm{Re}(\epsilon'/\epsilon)$ while still being able to do the vast amount of other physics mentioned in the previous chapter.[3] The detector requirements are:

1. Collect enough statistics
2. Measure the path length of the K_S, K_L decays to the required accuracy
3. Reject backgrounds at the desired level
4. Be self-calibrating, using various K decay modes, in addition to Bhabha scattering events.

Its scale is driven by a fundamental parameter, the mean decay path length of the long lived K^0-meson $L(K_L)$: at DAΦNE, $\beta(K)$=0.216 and $L(K_L) = \gamma\beta c\tau = 3.44$ m.

3.3 THE KLOE COLLABORATION

To be added in 1995 are collaborators from IHEP Beijing, China, Tel-Aviv University, Israel; and ITEP, Moscow, Russia.

A. ALOISIO[e], A. ANDRYAKOV[b], A. ANTONELLI[b], M. ANTONELLI[b], F. ANULLI[b], C. AVANZINI[h], D. BABUSCI[b], C. BACCI[j], R. BALDINI-FERROLI[b], G. BARBIELLINI[m], M. BARONE[h], K. BARTH[c], V. BATURIN[e], H. BEKER[h], G. BELLETTINI[g], G. BENCIVENNI[b], S. BERTOLUCCI[b], C. BINI[h], C. BLOISE[b], V. BOCCI[i], V. BOLOGNESI[g], F. BOSSI[b], P. BRANCHINI[k], L. BUCCI[h], A. CALCATERRA[b], R. CALOI[h], P. CAMPANA[b], G. CAPON[b], M. CARBONI[b], G. CATALDI[d], S. CAVALIERE[e], F. CERADINI[j], L. CERRITO[i], M. CERÙ[h], F. CERVELLI[g], F. CEVENINI[e], G. CHIEFARI[e], G. CIAPETTI[h], M. CORDELLI[b], P. CRETI[d], A. DORIA[e], F. DONNO[b], R. DE SANGRO[b], P. DE SIMONE[b], G. DE ZORZI[h], D. DELLA VOLPE[e], A. DENIG[c], G. DI COSIMO[h], A. DI DOMENICO[h], E. DRAGO[e], V. ELIA[d], O. ERRIQUEZ[a], A. FARILLA[a], G. FELICI[b], A. FERRARI[g], M. L. FERRER[b], G. FINOCCHIARO[b], D. FIORE[e], P. FRANZINI[h,f], A. GADDI[b], C. GATTO[e], P. GAUZZI[h], E. GERO[b], S. GIOVANELLA[h], V. GOLOVYATUK[d], E. GORINI[d], F. GRANCAGNOLO[d], W. GRANDEGGER[b], E. GRAZIANI[k], U. v. HAGEL[c], R. HAYDAR[b], M. IMHOF[c], M. INCAGLI[g], C. JORAM[c], L. KEEBLE[b], W. KIM[l], W. KLUGE[c], F. LACAVA[h], G. LANFRANCHI[h], P. LAURELLI[b], J. LEE-FRANZINI[b,l], A. MARTINI[b], A. MARTINIS[m], M. M. MASSAI[g], R. MESSI[i], L. MEROLA[e], A. MICHETTI[h], S. MISCETTI[b], S. MOCCIA[b], F. MURTAS[b], M. NAPOLITANO[e], A. NISATI[h], E. PACE[b], G. F. PALAMÀ[d], M. PANAREO[d], L. PAOLUZI[i], A. PARRI[b], E. PASQUALUCCI[i], M. PASSASEO[h], A. PASSERI[k], V. PATERA[b], F. PELUCCHI[b], E. PETROLO[h], M. C. PETRUCCI[h], M. PICCOLO[b], M. POLLACK[l], L. PONTECORVO[h], M. PRIMAVERA[d], F. RUGGIERI[a], P. SANTANTONIO[b], R. D. SCHAMBERGER[l], A. SCIUBBA[h], F. SCURI[m], A. SMILZO[e], S. SPAGNOLO[d], E. SPIRITI[k], C. STANESCU[k], L. TORTORA[k], P. M. TUTS[f], E. VALENTE[h], P. VALENTE[b], G. VENANZONI[g], S. VENEZIANO[h], X. L. WANG[b], S. WESELER[c], R. WIESER[c], S. WÖLFLE[b], A. ZALLO[b]

[a] Dipartimento di Fisica dell'Università e Sezione INFN, Bari
[b] Laboratori Nazionali di Frascati dell'INFN, Frascati
[c] Institut für Experimentelle Kernphysik, Universität Karlsruhe
[d] Dipartimento di Fisica dell'Università e Sezione INFN, Lecce
[e] Dipartimento di Scienze Fisiche dell'Università e Sezione INFN, Napoli
[f] Physics Department, Columbia University, New York
[g] Dipartimento di Fisica dell'Università e Sezione INFN, Pisa
[h] Dipartimento di Fisica dell'Università e Sezione INFN, Roma I
[i] Dipartimento di Fisica dell'Università e Sezione INFN, Roma II
[j] Dipartimento di Fisica dell'Università di Roma III e Sezione INFN, Roma I
[k] Istituto Superiore di Sanità and Sezione INFN, ISS, Roma.
[l] Physics Department, State University of New York at Stony Brook.
[m] Dipartimento di Fisica dell'Università e Sezione INFN, Trieste/Udine

3.4 Systematics Constraints

Since the observation[22] in 1964 that the long lived K^0 meson decays into two pions, the search for direct CP violation has failed. In terms of physical observables, if the direct CP violating amplitude $\langle\pi\pi|K_2\rangle$, where K_2 is CP-odd, vanishes, then:

$$\mathcal{R}_S \equiv \frac{\Gamma(K_S \to \pi^+\pi^-)}{\Gamma(K_S \to \pi^0\pi^0)} = \mathcal{R}_L \equiv \frac{\Gamma(K_L \to \pi^+\pi^-)}{\Gamma(K_L \to \pi^0\pi^0)}, \tag{3.1}$$

otherwise, in general, $|\mathcal{R}_S - \mathcal{R}_L| = \Delta\mathcal{R} \neq 0$ and $-\Delta\mathcal{R}/\mathcal{R}- = 6\times|\mathrm{Re}(\epsilon'/\epsilon)|$.

The aim of KLOE to reach a sensitivity in $\Delta\mathcal{R}/\mathcal{R}$ of $\sim 6\times10^{-4}$, which as mentioned in the previous chapter, from the statistical point of view, is achievable at DAΦNE at full luminosity in about one year. The two formidable tasks for KLOE to face are the controlling of efficiencies for the decays of interest and the rejection of background from the copious K_L decays to states other than two pions. At DAΦNE direct CP violation can also be observed by kaon interferometry of the two pion final states, as described before. However, some of the systematic uncertainties are the same for the two methods, and since their effect on the ratios defined in eq. (3.1) is slightly more intuitive, we will limit our present discussion to this case.

3.5 Measuring the two pion BR's

The relation between measurements and BR's, assuming tagging is used, is:

$$\underbrace{N^{\pm,0}_{L,S}}_{\text{observed}} - \underbrace{BK^{\pm,0}_{L,S}}_{\text{estimated}} = \underbrace{N_{K\bar{K}} \times \varrho_{L,S}(\text{tag})}_{\text{drops identically}} \times \underbrace{BR^{\pm,0}_{L,S}}_{\text{desired}} \times \underbrace{\left\langle \varrho^{\pm,0}_{L,S} \right\rangle}_{\langle\text{efficiency}\rangle} \times \iint_{\text{FV}} g(l-l')I(l)\,\mathrm{d}l\,\mathrm{d}l' \tag{3.2}$$

The double integral is a convolution of the decay intensity $I(l)$ and the experimental resolution $g(l-l')$ in the measurement of the decay path length and an integration over the fiducial volume, FV, of the detector. The implications of detector size, knowledge of the boundary of the fiducial volume and magnetic field value are discussed in this section. The four backgrounds $BK^{\pm,0}_{L,S}$ and the averaged efficiencies $\left\langle \varrho^{\pm,0}_{L,S} \right\rangle$ are different. They must be known to an accuracy of $\mathcal{O}(1/3000)$.

3.6 Fiducial Volumes

As will be described later, we assume a detector consisting of an electromagnetic calorimeter, a large tracking chamber and a vertex detector. The calorimeter has a central part which can be approximated as a cylinder of 2 m radius and 3.5 m length closed by two end caps, covering $\sim$98% of the solid angle. The chamber, with inner wall of 25 cm radius, provides tracking for $30 < r < 200$ cm. The whole detector is immersed in a solenoidal field of 0.6 T. Regeneration in walls (beam pipe, chamber walls) is $\leq$1% . Use of a large beam pipe, inside which all K_S's decay, and rejection of K decays up to 6 cm (10 τ_S) past any wall eliminate the effects of $K_L \to K_S$ regeneration. The fiducial volume (FV) for K_S and K_L decays are idealized below in fig. 7.

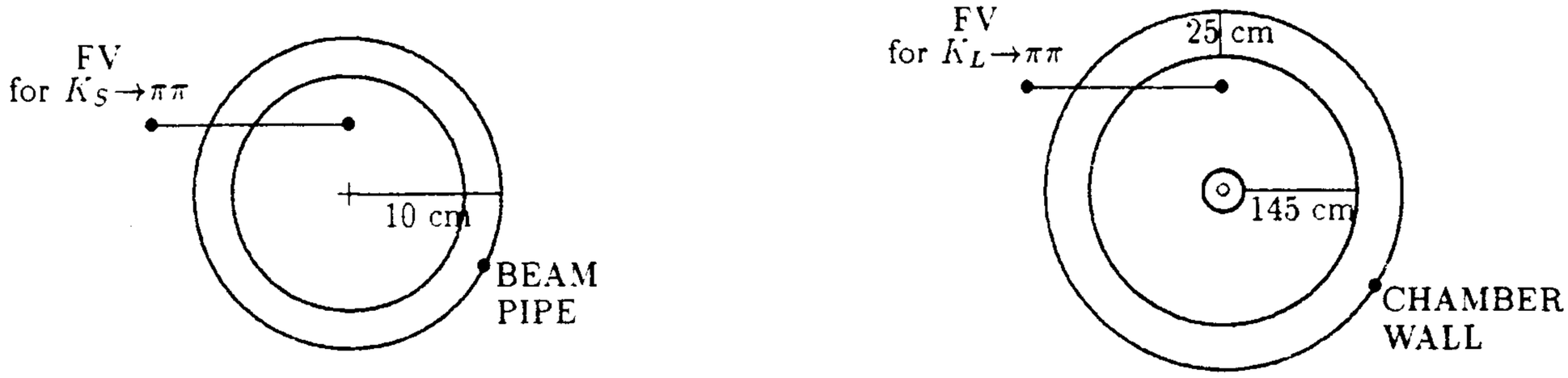

Fig. 7. Fiducial Volumes for K_S and K_L decays.

A beam pipe of 10 cm radius provides a vacuum region in which all K_S's decay. The helium based chamber is both the decay volume for K_L's and measures angle and momenta for charged particles. The fiducial volume for K_L decays, in cylindrical coordinates, is taken as:

$$\begin{aligned} 30 < r < 175 \text{ cm} \\ -125 < z < 125 \text{ cm} \end{aligned} \qquad (3.3).$$

3.6.1 K_S decay fiducial volume.

If the integral of equation (3.2) can be carried out to infinity. FV boundary and resolution do not contribute any error. This is essentially the case for K_S decays. A K_L signal guarantees the presence of a K_S. The beam pipe has radius equivalent to $\geq$13–17 lifetimes. Therefore without imposing, ideally, any fiducial volume cut on the data, the integrals are "1", independently of flight path resolution. Efficiencies for $\pi^+\pi^-$ and $\pi^0\pi^0$ decays are $\geq$99% and are well controlled. Backgrounds are at the level of 10^{-3}, before any cuts are applied.

3.6.2 K_L decay fiducial volume.

The case is quite different for K_L decays, since the fiducial volume has dimensions, ~145 cm, which is a small fraction of the mean decay path, ~350 cm. A small error on the determination of the boundary of the fiducial volume can introduce large errors on R_L, at the accuracy of interest. In particular what is relevant is the relative error in the determination of the boundaries of the fiducial volumes for $K_L \to \pi^+\pi^-$ and $K_L \to \pi^0\pi^0$, since different methods are used to obtain the K_L path length. $K_L \to K_S$ regeneration at chamber inner wall provides infact an excellent check of the correct knowledge of the inner boundary of the fiducial volumes. Observation of the enhanced $\pi^+\pi^-$ and $\pi^0\pi^0$ signals from K_S decays from the same source provides the required check. The outer boundary requires more care. Assuming a spherical fiducial volume defined by $30 < R < R_{FV}$ cm, the fractional change in detected events per unit change in R_{FV} is:

$$\frac{\delta N/N}{\delta R_{FV}} = \frac{1}{350} \times \frac{1}{\exp((R_{FV} - 30)/350) - 1} \text{ cm}^{-1}$$

For $R_{FV}=\infty$ the error on $\delta N/N$ vanishes. For R_{FV}=150 cm, $\delta N/N \sim 1\%$ for δR_{FV}=1 cm, while for R_{FV}=500 cm the fractional error on N is 10 times smaller, however practically not realizable. A reduction on detector radius of 20%, from the one given above, implies a reduction in fiducial volume of a factor 2 and an increase in the fractional error of a factor three. We are much less sensitive to uncertainties in the z-boundary because of $\sin^2\theta$ production angular distribution. The argument above justifies our choice for the detector size in the sense that it is the value for which the fractional change in $(1/N)(\delta N/\delta R_{FV})$ equals the fractional change in detector volume.

To achieve a sensitivity of 6×10^{-4} in $\Delta\mathcal{R}/\mathcal{R}$, we must insure that the outer boundaries of the fiducial volumes for charged and neutral decays are equal to better then 0.5 mm. The most effective way to ensure this is to use K_L decays for which both a "neutral" and a "charged" decay vertex is measurable such as $K_L\to\pi^+\pi^-\pi^0$. Decays of charged K's, $K^\pm\to\pi^\pm\pi^0$, can also be used over part of the FV, see section on calibration.

3.7 Backgrounds

The main sources of background in CP experiments are the non CP violating decays of K_L. The $\pi^0\pi^0\pi^0$, $\pi^+\pi^-\pi^0$, $K_{\mu3}$, and K_{e3} modes which are ~100 times more abundant. The rejection of $\pi^0\pi^0\pi^0$ relies on good solid angle coverage and efficiency for γ's down to 20 MeV energy, which we will achieve in correct calorimeter design. The rejection of $\pi^+\pi^-\pi^0$ is easier because the probability of losing 2/2 γ's is 15 times smaller than losing 2/6 γ's, in addition we will have help from chamber measurements of the charged tracks.

A realistic study of the methods for removing $K_{\mu3}$ contamination has been developed. A large sample, 1.35×10^7 $K_{\mu3}$ and 10^5 $K_L\to\pi^+\pi^-$ events, was generated using the standard size of the luminous region, $\sigma_x = 0.2$ cm, $\sigma_y = 20$ μm, $\sigma_z = 3$ cm. $K\to K_{\mu3}$ and $K\to\pi^+\pi^-$ events are distinguished by the use of a χ^2 function constructed using the measured variables corresponding to the all kinematical constraints available. A double Gausssian parameterization has been applied to the resolution functions (in p_T, ϕ, $\cot(\theta)$, vertex position) obtained from reconstructed GEANFI[23] generated tracks, using the ARGUS–KLOE program for a 84 layer stereo chamber, to take tails into account. The χ^2 function is peaked at very low values for $K_L\to\pi^+\pi^-$ decays, while for $K_{\mu3}$ events it vanishes at 0 and extends to very high values. This calculation has been repeated for several values of the magnetic field, 4 to 8 kG. The rejection factor at 6 kG is approximately 4.5×10^{-4} with a $\pi^+\pi^-$ signal efficiency of 98.8%.[20] The K_{e3} decays are more easily distinguished and removed because partly $m_e \ll m_\mu$ and the energy deposition pattern of an electromagnetic shower in the calorimeter is very distinctive.

3.8 Trigger

Triggering at DAΦNE will be an entirely new experience. At full luminosity, the ϕ–event rate is ~5 kHz while the machine produced background when properly masked, can be estimated, scaling from other machines to be ~10% of this value. All events in principle must be passed to the digitizing electronics (FEE) and data acquisition system (DAQ). The calorimeter can provide an adequate trigger for most events of interest, especially when complemented with some tracking information.

Bhabha scattering at angles $10°< \theta <20°$and cosmic ray events must be recognized and rejected or prescaled not to overload FEE and DAQ. Both these two classes of events are important for detector calibration. We will employ calorimeter information and simple combinatorial logic to reject/scale these events.

3.9 Calibration

At DAΦNE a general purpose detector capable of measuring all decay modes of the ϕ has a wealth of processes useful for the calibration of its efficiencies. Furthermore the availabilty of

abundant Bhabha scatterings observed in the detector allows a complete calibration of energy and time scales. The following table summarizes the accuracies to which the key parameters can be monitored by various methods. We conclude that KLOE is truly a "self-calibrating" detector!

Table 5. Detector Calibration

Parameter	Method, Process	Accuracy/ minute
Energy Scale	Continuous, absolute, BHABHA	1%/cluster
Time Scale	Continuous, absolute, BHABHA	$12ps$/cluster
Tracking Efficiency	Continuous, absolute, e^+e^-, $\mu^+\mu^-$, $K \to$ 3body	10^{-3}/track
Photon Efficiency	Continuous, absolute, $K^{\pm} \to \pi^{\pm}\pi^0$, $K^0 \to \pi^+\pi^-\pi^0$	10^{-3}/cluster
F.V. $\pi^0\pi^0/\pi^+\pi^-$	Continuous, relative, $K^{\pm} \to \pi^{\pm}\pi^0$, $K^0 \to \pi^+\pi^-\pi^0$	10^{-3}/global

3.10 Data Acquisition

ϕ decays and calibration events represent, at full DAΦNE luminosity, a very large load for the data acquisition system. At 10,000 events per second, each event consisting of 2 to 4 kBytes, we estimate that 20,000 MIPS equivalent computing power will be necessary to digest the data. The universal approach appears to be farms of the new powerful μ-processors. We are looking at the α-VAX product of DEC, capable of 120 MIPS, amongst possible choices. We intend to write to tape all raw data, and we need to perform Monte Carlo simulations at the 10^8 or greater, event level. The data produced in one year at full $\mathcal{L}$ is $\sim 4 \times 10^{14}$ Bytes, to be stored at a bandwidth of 50–100 MBytes/s. The new Digital Linear Tapes, DLT by DEC, seems capable of such task. Due to the Monte Carlo simulation needs and the inevitable necessity of running production more than once we plan on two 20,000 MIPS farms.

4. THE KLOE DETECTOR

4.1 Overview

From the discussions of the previous chapter we conclude that KLOE must be able to track charged particles of momenta between 50 and 250 MeV/c. It must also detect with very high efficiency γ's with energy as low as 20 MeV, measure their energies with a resolution $\delta E_\gamma / E_\gamma \sim 15\%$ at 100 MeV and provide the space coordinates of the photon conversion point so that the K_L decay path can be determined to within ~1 cm. Thus while the general features of the KLOE detector are similar to those of a *typical* general purpose collider's apparatus: a cylindrical structure surrounding the beam pipe, consisting of a highly efficient, large tracking device for detecting the charged K^0 decay products, an electromagnetic calorimeter with exceptional timing ability, which also provides some particle identification, all enclosed in a solenoidal field, each component has its own unusual features. The KLOE cross section is shown in fig. 8. We discuss the components, in order of increasing radius.

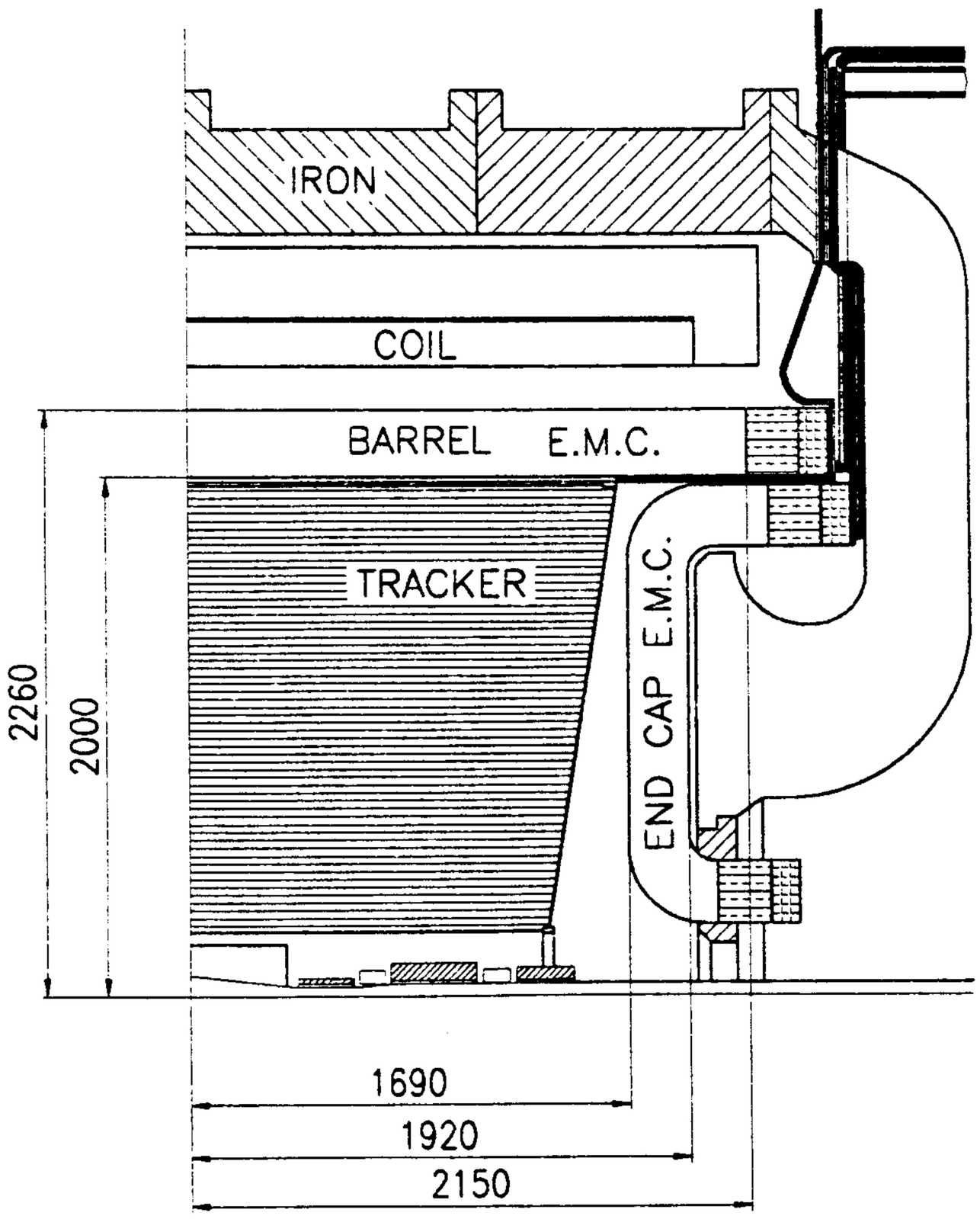

Fig. 8. KLOE cross section along the beam axis.

4.2 Beam Pipe

The radius of the beam pipe around the luminous point is 10 cm. This allows the definition

of a fiducial region for K_S decays without complication from regeneration. The beam pipe is made of 0.5 mm thick beryllium to minimize multiple scattering, energy loss for charged kaons and regeneration. The enlargment of the beam pipe at the interaction point, visible in fig. 8 as a trapezoidal structure, is in fact a technical challenge for DAΦNE because it could act as a free wheeling RF cavity, with all the attending problems. In figure 8 we also show that the low β insertion permanent magnets are mounted directly on the beam pipe, inside KLOE, another difficult technical problem to be solved.

4.3 Tracking Chamber.

Identification of decays into charged particles requires tracking over the decay drift space. Tracking is performed in a large drift chamber, 3.5 m long and 4 m in diameter, employing helium (90%He + 10%Isobutane) gas to reduce regeneration and multiple scattering. The use of helium for tracking chambers is well demonstrated, though perhaps not over as large a volume as KLOE. Unique to KLOE is the need of a uniform cell structure, because the K_L decay vertices are uniformly distributed in distance from the luminous point. Walls must be very thin to provide good transparency for the photons from decays into π^0's to reach the electromagnetic calorimeter which surrounds the drift volume. The end plates will have a spherical shape to provide rigidity under the tension from 50,000 some wires. Details are found in the tracking chamber chapter.

4.4 Electromagnetic Calorimeter.

Reconstruction of the $\pi^0\pi^0$ decay mode of a 110 MeV/c momentum K, the determination of its decay point and the efficient rejection of the three π^0 decays make designing the electromagnetic calorimeter, EmC, a most challenging project. Unique to the KLOE experiment, is the method of determining the flight path of K_L, the segment ID in fig. 9, by time measurements. I is the ϕ decay point, the direction of ID is given by $-\mathbf{p}_{K_S}$, and A is the photon conversion apex in the calorimeter. As illustrated in fig. 9, the flight time measurements for even a single photon of the four from $\pi^0\pi^0$'s allow the determination of the K_L decay path. The time of arrival of a photon gives the flight path of the K^0 to an accuracy $\delta l = \beta_K c\,\delta t \sim 6 \times 10^{-3}$ cm $\times\, \delta t$(ps). For a 510 MeV K^0, that is for four photons with $\sum E_\gamma = 510$ MeV one expects a time resolution of ~100 ps and a path resolution of 0.6 cm. Observation of only three out of four photons still allows an over constrained determination of both the K^0 mass and the flight path, using time, position and energy measurements.

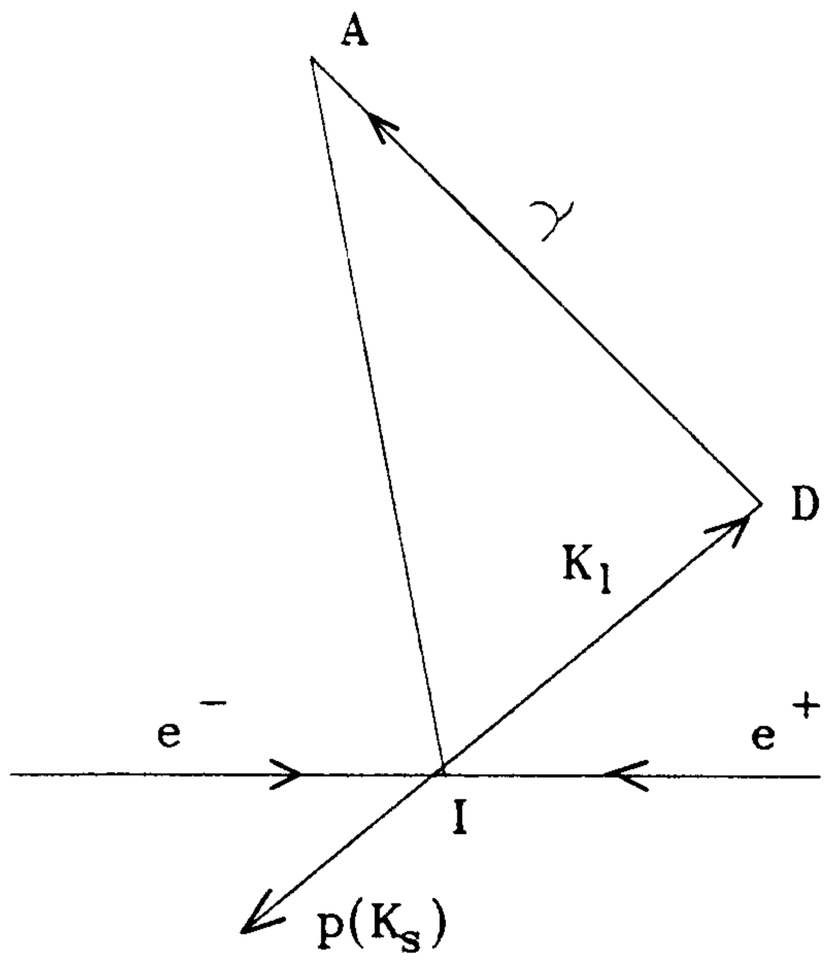

Fig. 9. Measuring the K_L decay length.

Partial KLOE views are shown in figure 10. The top figure shows an endview of the top half with half of the return iron yoke cut away, the lower figure shows a side view, again with half of the iron yoke cut away. The details of the calorimeter design is in the following chapter.

4.5 Magnet

Of crucial importance in rejecting contamination of the $K_L \to \pi^+\pi^-$ sample is the ability of performing good measurements of momenta in the range 155–268 MeV/c In particular $K_{\mu 3}$ decays overlap kinematically $K_L \to \pi^+\pi^-$ decays when the laboratory muon momentum is ~250 MeV. A simple arguments predicts that kinematical overlaps decrease as the cube of the field value. This has been proved by full Monte Carlo calculations. A possible arguments against high field is the loss of tracking efficiency and accuracy in vertexing for spiraling tracks. Again we barely see a loss in tracking efficiency beginning at 7 kG, ~0.2% as well as some saturation in the $K_{\mu 3}$ background rejection. This justify our choice of 6 kG, which provides good rejection without impairing other detector functions.

The chamber and calorimeter are inside a superconducting coil and the iron return yoke has deep cavities hollowed out so that the magnetic field therein is reduced and axial, to allow proper funtioning of the mesh photomultipliers employed in the EmC readout. Economical ons, *i.e.* power consumption, made a superconducting coil the choice of interest.

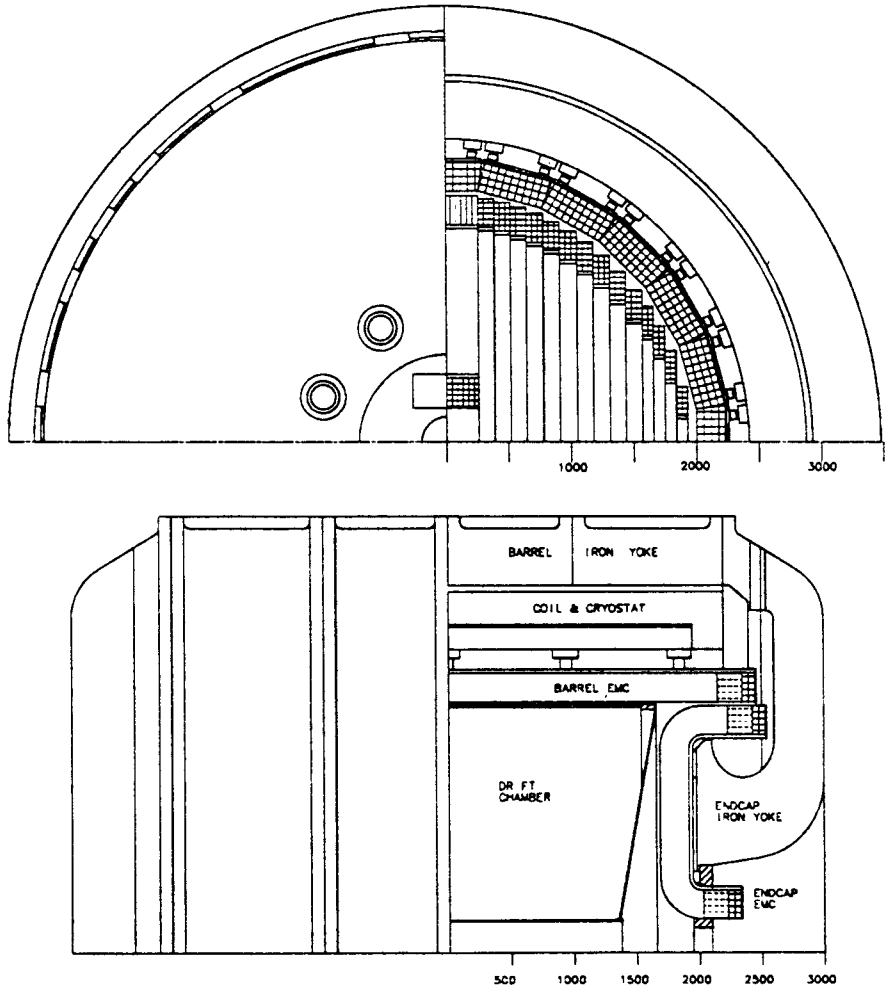

Fig. 10. Partial KLOE views.

5. CALORIMETER

The KLOE EmC is a very fine sampling lead-scintillating fiber calorimeter, with photomultipliers, PMs, read-out. The central part, barrel, approximates a cylindrical shell of 4 m inner diameter, 4.3 m active length and 23 cm thicknes. The barrel covers the polar angle region $49° < \theta < 131°$ and consists of 24 sectors with trapezoidal cross section, ~60 cm wide. Two end-caps, 4 m in diameter and 23 cm thick, close hermetically the calorimeter. Each end-cap, consists of 26 "C" shaped modules which run vertically along the chords of the circle inscribed in the barrel. At the two ends they are bent at 90°, becoming parallel to the barrel ends, to decrease the effects of the magnetic field on the PMs and to increase hermeticity, see figures 8 and 10. In our EmC fibers run mostly transversely to the particle trajectories. This reduces sampling fluctuations due to channeling, resulting in improved resolution particularly important at low energies.

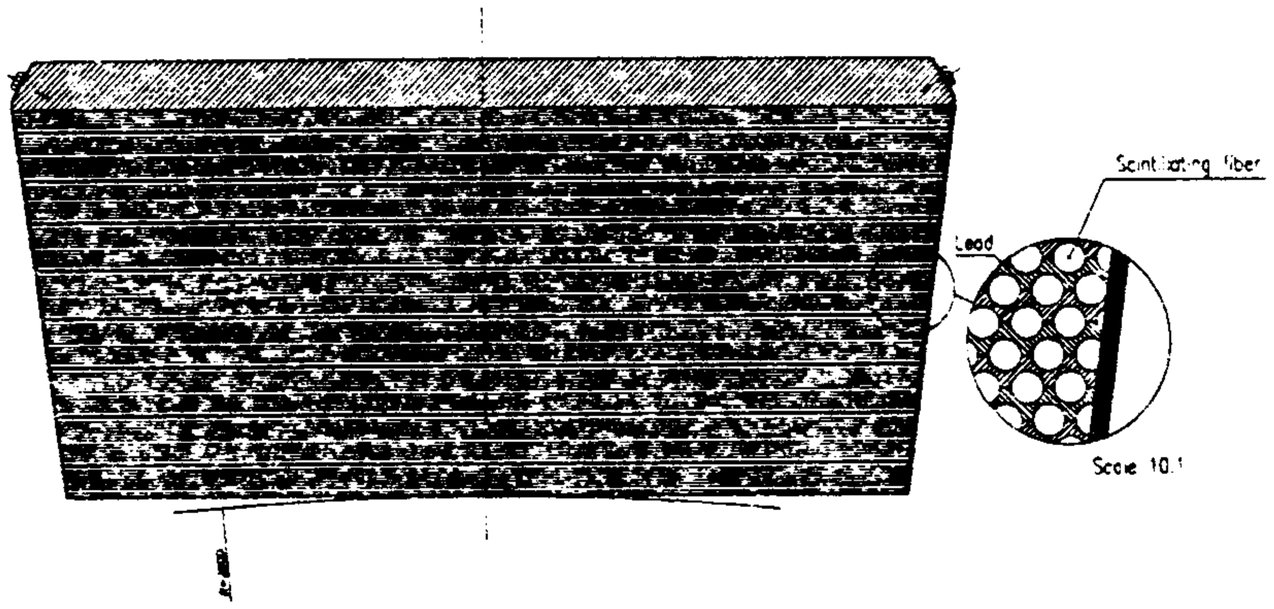

Fig. 11. Fiber and lead layout.

Each module of the KLOE EmC is built by glueing 1 mm diameter blue scintillating fibers between thin grooved lead plates, obtained by passing 0.5 mm thick lead foils through rollers of proper shape. The grooves in the two sides of the lead are displaced by one half of the pitch so that fibers are located at the corners of adjacent, quasi-equilateral triangles resulting in optimal uniformity of the final stack, see fig. 11. The grooves are just big enough to insure that the lead does not apply direct pressure on the fibers. Light travelling in the cladding is effectively removed because of the glue surrounding the fibers. The selected fiber pitch of 1.35 mm results in a structure which has a fiber:lead:glue volume ratio of 48:42:10 and a sampling fraction of ~15% for a minimum ionizing particle. The final composite has a density of ~5 g/cm^3 and a radiation length X_0 of ~1.6 cm, is self supporting and can be easily machined. The very small lead foil thickness ($< 0.1\,X_0$) results in a quasi–homogeneous structure and in high efficiency for low energy photons. Measurements indicate that the blue-green Kuraray SCSF-81, Bicron BCF-12 and Pol.Hi.Tech-46 fibers, satisfy our requirements for light yield, scintillation decay time and attenuation length.[24] Since the time resolution depends on the light yield, great care has been put in maximizing the efficiency of the light collection system and insuring uniform photocathode illumination. Each light guide consists of a mixing part and a Winston cone concentrator.[25] We are thus able to match the calorimeter elements to the PM photocathodes, with an area reduction factor of up to ~4, without losses, because of the small 22° divergence angle of the light travelling in the fibers.

5.1 Construction and tests of Prototypes

We built a *barrel* prototype module of dimensions 14×24×203 cm^3 to establish construction procedures and perform realistic tests of the final EmC performance, see fig. 12a). The module depth of 24 cm is equivalent to a thickness of 15 X_0, consisting of 207 lead and scintillating fiber layers for a total of 21,450 fibers. The first 3.5 cm are Kuraray SCSF-81 fibers followed by 20.5 cm of Kuraray SCSF-38 fibers. It weighs 330 kg. The module was made in the Frascati machine shop. The grooved lead foils were produced with a home-made rolling machine starting from 0.5 mm thick lead foils. The grooved rollers, made of hardened steel and ground to shape by a diamond tool, are mounted with ball bearings on a very rigid frame and are aligned and checked with a set of micrometers. Foils of almost 6 m length and 15 cm wide have been produced. The thickness uniformity obtained is around few tens of μm, the grooves deviate from a straight line by less than 0.1 mm per meter of foil length. The module was constructed by glueing the first lead foil to a 2 cm thick aluminum back plate carrying all the mounting fixtures. Bicron optical epoxy resin, BC 600 ml, was then applied in a precisely measured amount to the top surface of each lead foil. A layer of fibers was then laid down in the grooves and epoxy applied anew. Typically, 6–7 layers of fibers and lead were stacked in about one hour, before the glue started curing. The growing stack was then compressed under vacuum for at least 30 min to apply uniform pressure, and to squeeze out excess glue. Once the final thickness was reached the two ends were cut and milled. No fiber was damaged during the stacking phase, while four fibers were lost during the final milling. The calorimeter was wrapped in a 1 mm thick steel skin, in order to simulate the final design and provide protection for the module.

A prototype for the *end-cap* region, fig. 12b), consisting of two "C" shaped modules, was also built. The width of each module is 7 cm and they both have the same depth of 24 cm. Each section consists of a central straight piece (89–110 cm), two curved pieces with an inner radius of 7.5 cm, and two straight end pieces to which light guides are glued. The first 7 cm employ Kuraray SCSF-81 fibers, the rest are Pol.Hi.Tech-46 fibers. The structure was constructed by cutting the grooved lead foils and fibers to the desired lengths, incising at the two ends the central groove of each lead foil, leaving the central part uncut for a length of 89 cm, then bending the two adjacent modules.

The readout, identical for both prototypes, was organized into 22 elements for each side: five planes of four small elements, 3.5×3.5 cm^2, and two large rear elements, 6.5×7 cm^2, see fig. 12b). For the small elements light was transported from the calorimeter through light guides to 1-1/8 inch diameter PMs, with an area concentration factor of ~2.7. 1-1/8 inch Hamamatsu phototubes, type R1398 with a transit time spread of less than 1 ns have been used. The rear elements were similarly coupled to 5 cm diameter PMs, with an area concentration factor of ~2.5.

In order to investigate the effect of coarsening the readout granularity and using larger light guides, we took data with the *barrel* readout organized in four planes of three 4.2×4.2 cm^2 cells, leaving the last plane unchanged. This configuration is referred to as "coarse" granularity, see fig. 12a). Since the same PMs were used, the light guides had an area concentration factor of ~3.8.

Prototype Tests

The calorimeter prototypes have been tested[26,27] in a beam at the Paul Scherrer Institut, PSI, in Villigen, Switzerland. The PSI machine is an isochronous cyclotron which accelerates protons to 600 MeV kinetic energy. A secondary beam of π's, μ's and e's in the momentum range 50–400 MeV/c was delivered to the test areas.

Two crossed scintillators in front of the calorimeter and a third counter, 4.5 m away from the calorimeter, provided a beam trigger, defined the beam position at the calorimeter and enabled $\pi/\mu/e$ identification by time of flight, see fig. 13.

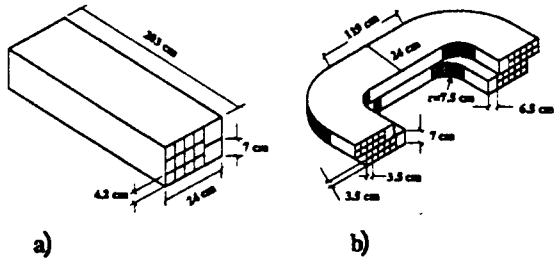

Fig. 12. a) *Barrel* and b) *end-cap* prototype.

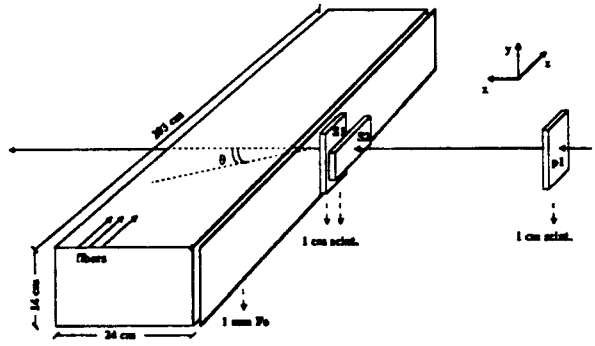

Fig. 13. Calorimeter test setup at PSI.

The calorimeter PM outputs were connected to active splitters through 5 m of RG-58 cable. The two outputs of each splitter were sent to CAMAC ADCs and to low threshold (5 mV) discriminators, the signal for 50 MeV being ~350 mV. The discriminator outputs acted as TDC stops. The trigger signal was used to generate the ADC gates and the reference time signal T_0 which supplied the "start" for the TDC system.

The *barrel* prototype has also been tested with tagged low energy photons (20–80 MeV) at the Frascati LADON facility.[28] At LADON photons are obtained by back scattering a laser beam from electrons stored in ADONE. A tagging system for the recoil electrons yields a determination of the photon energy with a resolution of ~1.7 MeV. The trigger was obtained by a coincidence from the two calorimeter ends, after adding all signals from each side. The trigger generated ADC gates and the TDC start signals which were cleared if there was no trigger from the tagging system within 200 ns.

Energy Response and Resolution

The coordinate system used in the data analysis is shown in fig. 13, where the definition of the incidence angle θ is also indicated. The origin was put in the center of the calorimeter

surface facing the beam.

In order to study the energy response of the prototype we define the total visible energy E_{vis} as the sum over all elements read out on both ends, labelled A and B. To correct for the response of each channel we divided the signal $E_{adc,i}$ of channel i, by the calibration constants $K_{mip,i}$: $E_{vis} = (1/2)\sum(E_{A,i}+E_{B,i})$ with $E_i = E_{adc,i}/K_{mip,i}$. The calibration constants $K_{mip,i}$ in ADC counts, were obtained with cosmic rays and 400 MeV/c pions, both of which are minimum ionizing particles to a first approximation, incident at the center of each element. Clean samples of events selected for the calibration were ensured by means of triggering and software cuts. A gaussian fit to the pulse height distribution was performed for each channel to determine the peak position. The fit interval was chosen to be asymmetric with respect to the mean value, to take into account the asymmetric shape of the distribution.

We define 1 MIP as the visible energy deposited by a minimum ionizing particle in a 3.5×3.5 cm^2 readout element; our simulation[29] determines 1 MIP to be equivalent to an average energy deposit of 3.24 MeV in the active material. For the coarse granularity and for the larger cells of the last plane geometrical correction factors have been used to express the results in our calibration units. Pions of 400 MeV/c momentum are minimum ionizing particles only in the first plane of the calorimeter. We have therefore corrected for the increase of the specific ionization with calorimeter depth and for straggling effects. The correction factors used for both granularities are given in table 6.

Table 6. Specific ionization correction factors.

Plane Number	1	2	3	4	5	6
3.5 × 3.5	1.00	1.03	1.04	1.06	1.10	1.14
4.2 × 4.2	1.01	1.04	1.05	1.09	1.14	-

Before reaching the calorimeter the beam had to pass through the trigger counters and the iron skin of the calorimeter itself. The total amount of material is equivalent to 3.6 cm of scintillator. Positrons lose ~7 MeV while the energy loss of pions and muons depends on their kinetic energy and was appropriately taken into account. These corrections have been applied to the beam energy of the charged particles.

The following results were obtained with positrons and photons entering the center of the calorimeter front face (z = 0 cm, θ = 0°). The distributions of the energy signal for photons ranging from 28 to 63 MeV are are displayed in fig. 14. From the very good symmetry of the line shape at the lowest energy of 28 MeV, we can conclude that at these energies, the calorimeter is still fully efficient.

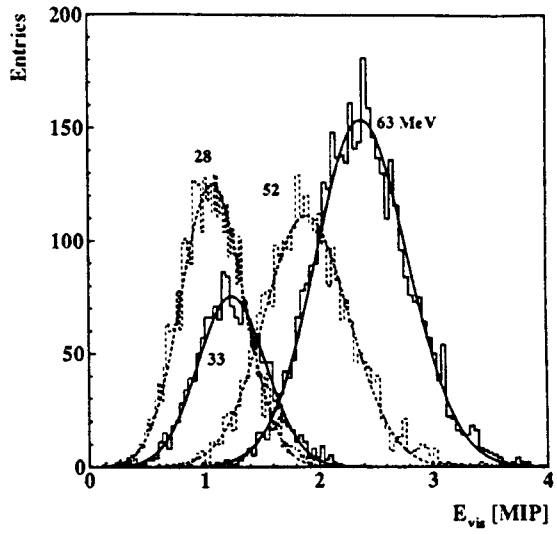

Fig. 14. Energy spectra for photons.

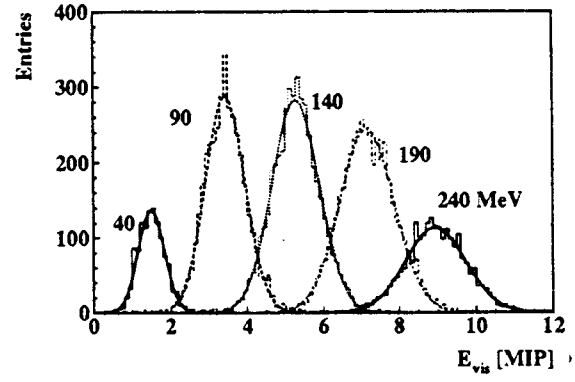

Fig. 15. Energy spectra for positrons.

For each spectrum a gaussian fit, leaving all three parameters free, has been performed; the mean of the fit was used as the average calorimeter response E_{vis} and the square root of the variance $\sigma_{E,vis}$ was used to compute the energy resolution. The plot of E_{vis}/E *vs.* the energy E have a maximum deviation from linearity of less than 3%, mostlty due to inaccuracies in the tagging system. The line shapes for positrons in the energy range 40–240 MeV are shown in fig. 15 for *barrel* data with the coarse granularity. The linearity of the response is excellent with a deviation of at most 2%, again mostly from beam setting inaccuracies.

Fitting photon and positron data together we obtain a slope $s_{barr} = (36.8 \pm 0.2)$ MIP/GeV, see fig. 16. In the same plot we have also added data for the *end-cap* prototype exposed to positrons (triangle symbols) for which the slope is $s_{ecap} = (37.4 \pm 0.6)$ MIP/GeV. The average response to electromagnetic (e.m.) showers is proportional to the incident particle kinetic energy only if the shower is fully contained. Simulations[29] show that the depth of the prototype keeps leakage below the 2% level for the energy range of interest. The sampling fraction for e.m. showers can therefore be estimated as $f_{em} = E_{vis}/E = (36.8 \pm 0.2)$ MIP/GeV$\times$3.24 MeV/MIP $= (11.9 \pm 0.1)\%$.

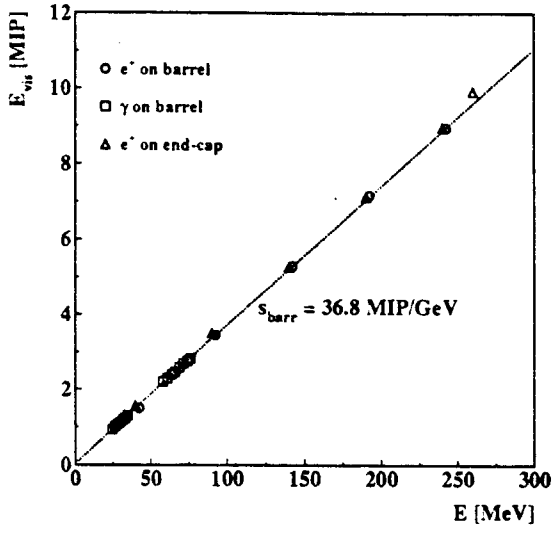

Fig. 16. Energy response for photons and positrons vs. kinetic energy.

The fluctuation of the ratio R between the energy signals, from each readout element, E_A and E_B at the two calorimeter ends, $R = E_A/E_B$, allows us to estimate the number of photoelectrons N_{pe} in each tube, from $N_{pe} = (\sqrt{2} \times \mu_R/\sigma_R)^2$, where μ_R and σ_R are the mean of R and the r.m.s. spread of its distribution respectively. For the *barrel* prototype the typical signal for a minimum ionizing particle at 1 m distance from the photomultiplier is ~65 pe. Results within 10% were obtained by measuring the PM gain directly. A lower light yield of ~50 pe/MIP is obtained in the *end-cap* prototype due to the worse quality fiber used in its construction. The y resolution for positrons is $\sigma_E/E = (4.47 \pm 0.02)\%/\sqrt{E\ (\mathrm{GeV})}$ and for photons $\sigma_E/E = (4.35 \pm 0.01)\%/\sqrt{E\ (\mathrm{GeV})}$. The measured resolution for positrons and γ's are shown in fig. 17. The $1/\sqrt{E}$ dependence indicates that sampling fluctuations and photoelectron statistics dominate the resolution. The contribution of the latter has been evaluated from the light yield to be $1.6\%/\sqrt{E}$ and is therefore negligible. A similar analysis for the *end-cap* gives an energy resolution of $\sigma_E/E = (4.59 \pm 0.04)\%/\sqrt{E(\mathrm{GeV})}$.

The response for muons and pions in the momentum range 150–280 MeV/c, of interest for the KLOE experiment, has also been studied. Due to their low kinetic energy (50–180 MeV) these particles lose energy mostly by ionization and could stop in the calorimeter. The response *vs.* kinetic energy for both types of particles is identical. A linear fit of the energy response curve gives a slope s_μ=46.8 MIP/GeV, corresponding to a sampling fraction for muons of $f_\mu = E_{vis}/E = 46.8 \pm 0.4$ MIP/GeV $\times$ 3.24 MeV/MIP $= 15.2 \pm 0.1\%$ and an "e/μ" ratio of f_e/f_μ=0.79. The energy resolution does not scale perfectly with $1/\sqrt{E}$ because sampling fluctuations become larger near the end of the particle's range. However, an approximate parametrization of the resolution is given by $3.7\,\%/\sqrt{E}$.

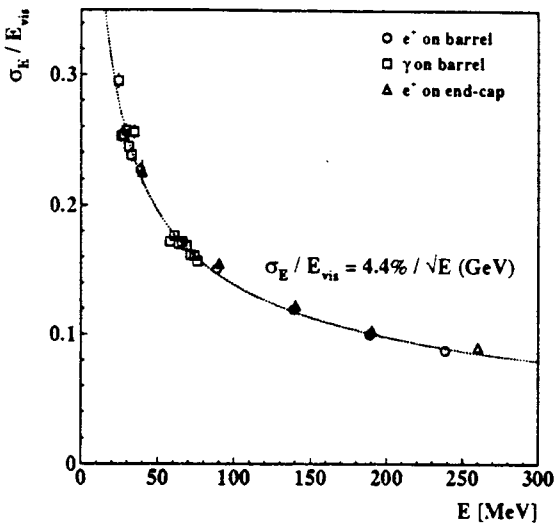

Fig. 17. Energy resolution for photons and positrons vs. kinetic energy.

A z–scan along the module axis was performed with 200 MeV/c positrons at seven different z–positions from −80 to +80 cm. The z dependence of the signal is well represented as $E_{vis}(z) = E_{vis}(0)\cosh(z/\lambda)$, due to adding two exponentials, with an attenuation length λ=240 cm, while the resolution is constant. The response of the barrel prototype as a function of the incidence angle, θ, has been studied using photons, positrons and muons at 30°, 45° and 60° incidence. Response and resolution do not depend on θ as expected for a quasi homogeneous calorimeter with very thin converter layers. For low energy photons, E <60 MeV, we observe a small worsening of the resolution, ~25%, at θ = 60°. The curved parts of the end-cap prototype have been investigated by scanning the prototype with 200 MeV positrons incident at 45° at different positions, moving along the outer surface of the bent part. No appreciable variation was found in the scan.

Timing Performances

The particle arrival time in the calorimeter is given, for each PM, by a discriminator output, used as a TDC "stop". For charged particles, the common "start" of the TDC system was obtained from the beam defining counters. For photons we self triggered on the analog sum of all calorimeter signals, as mentioned previously. Time walk correction depending on pulse height were applied off-line. The times measured at each calorimeter end T_A, T_B are obtained by the energy weighted average over all elements: $T_A = \sum E_{A,i}T_{A,i}/\sum E_{A,i}$; $T_B = \sum E_{B,i}T_{B,i}/\sum E_{B,i}$. The average of T_A and T_B then defines the mean arrival time T. For photons we perform our analysis in terms of the time difference $\Delta T = (1/2)\sum E_i\,(T_{A,i} - T_{B,i})/\sum E_i$, ΔT and T are the difference and sum of T_A and T_B and therefore have the same r.m.s. spreads, *i.e.* $\sigma_{\Delta T}$=σ_T except for the fact that the "start" time jitter is cancelled event by event in ΔT while it has to be unfolded for the external trigger case.

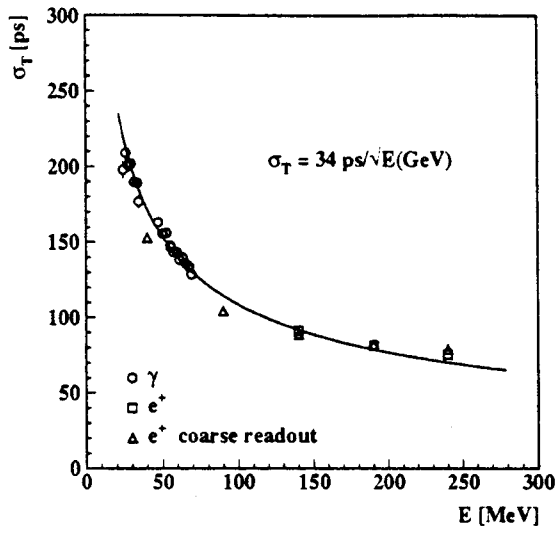

Fig. 18. Time resolution vs. energy.

The dependence of $\sigma_{\Delta T}$ on beam energy for 20–80 MeV γ's and of σ_T for 50–250 MeV positrons, at normal incidence on the calorimeter surface, are shown together in fig. 18, corresponding to a time resolution of $\sigma(T \text{ or } \Delta T)$=34 ps/$\sqrt{E\ (\text{GeV})}$. Fitting all measurements of $\sigma_{\Delta T}$ from 20 to 250 MeV gives $\sigma_{\Delta T}$=36 ps/$\sqrt{E\ (\text{GeV})}$, in excellent agreement with the result requiring unfolding of the "start" uncertainty. The measurements of the time resolution with a coarser readout granularity, (4.2×4.2 instead of 3.5×3.5 cm^2) triangle symbols in fig. 18, are indistinguishable although the light guides area reduction factor increases from 2.7 to 3.8, showing that light collection efficiency is unchanged. For the end-cap prototype we find a time resolution of σ_T =40 ps/$\sqrt{\text{E(GeV)}}$, with 50–200 MeV positrons.

The dependence of σ_T on θ was studied for all available beam energies. At 60° the resolution for 250 MeV positrons is ~25% worse than the result for normal incidence. The distributions are still gaussian. At lower energies the angular dependence of the resolution becomes negligible, being dominated by electron statistics. The investigation of the curved portion of the end-cap prototype as described, found no dependence. Only for the most extreme conditions, when the shower effectively crosses the fibers twice, the time resolution deteriorates by ~20%.

All our measurements confirm that the time resolution scales as the number of photons to the $-1/2$ power. We therefore expect that the resolution is best at the center of the calorimeter. The z dependence of the time resolution is given by: $\sigma_T(z) = \sigma_T(0)\sqrt{\cosh(z/\lambda)}$. This has been verified with the data from the z-scan. The resolution at the two ends of the barrel module is ~1.05 times worse than at the center.

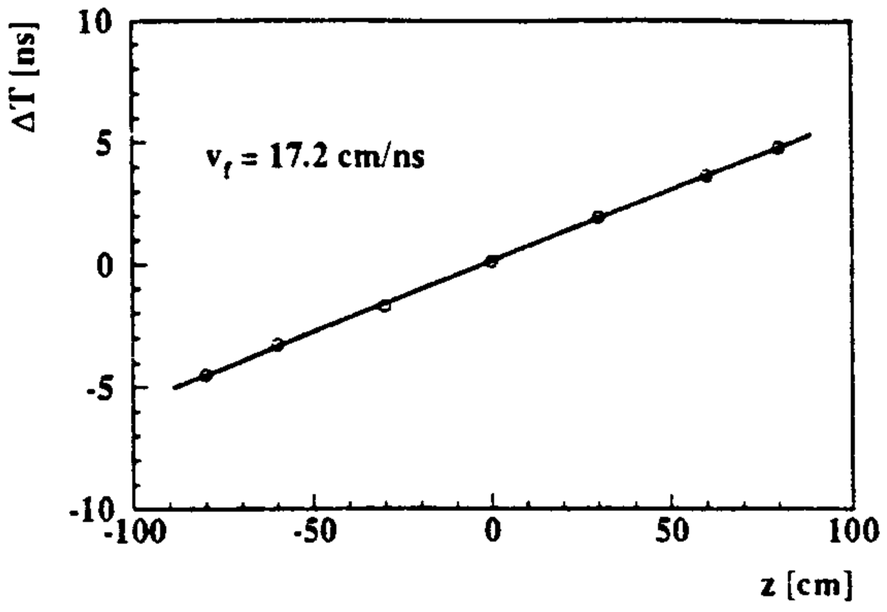

Fig. 19. ΔT distribution vs. nominal z-position for 200 MeV positrons.

Measurement of the z–Coordinate

The z–coordinate of the entry point z_e obtained from the time difference ΔT and the effective light propagation speed in the fibers v_f is: $z_e = v_f \Delta T$. ΔT is plotted *vs.* the nominal z position in fig. 19. From a fit to the data we obtain v_f=17.2 cm/ns, in agreement with the refractive index of the fiber core, n=1.6, and the bounce angle in the fiber. The position resolution σ_z, given by $\sigma_z = v_f \sigma_{\Delta T}$ is σ_z=6 mm/$\sqrt{E\ (\mathrm{GeV})}$ for the e.m. showers.

5.2 Particle Identification

$K_L \to \pi\mu\nu$ decay, $K_{\mu 3}$, constitutes the most significant background to the identification of $K_L \to \pi^+\pi^-$ decays. The calorimeter can provide some π/μ identification to improve the background rejection from kinematics.[20] π/μ identification can be obtained by time of flight, Monte Carlo studies[4] show that the time resolution of the KLOE calorimeter, combined with tracking information result in a $K_{\mu 3}$ rejection factors of 5–6, with 93% signal efficiency. π/μ identification can also be achieved by studying the energy signals and the first and second moments of the energy deposition distributions in the calorimeter. This method has been tested with data collected for pions and muons of 200–250 MeV/c, a $K_{\mu 3}$ rejection factor of 5 for is obtained while maintaining an efficiency of 95% for pions.

5.3 Module Ø

All the machinery for building the *barrel* calorimeter have been designed and built by the KLOE calorimeter group, mostly at LNF. The first full size *barrel* module, with dimensions of 23 cm×60 cm×430 cm and trapezoidal cross section, called module Ø, was then succesfully built, also at Frascati. The machinery has been turned over to a company which will assemble all modules of the *barrel* calorimeter. The front half of module Ø is built with Kuraray SCSF-81 fibers and the back half with Pol.Hi.Tech-46 fibers.

The module read out consists of five planes of 12 elements each, of ~4.4×4.4 cm^2, varying slowly in size across the module face. Each element is viewed through light pipes which provide mixing and terminate with a Winston concentrator coupled to mesh photomultipliers. The PMs are manufactured to KLOE specifications by Hamamatsu (R2021, mod.). KLOE needs to use these special tubes because they can operate in moderate magnetic field.[30] As shown in fig.

8, they are inside the return yoke where they see up to 0.15 T inclined less than 25° with respect to the PM's axis.[31] These PMs have a measured quantum efficiency of only ~60% of the conventional tubes like the ones used in the previous prototypes.[32]

Module Ø employs the final KLOE electronics. The PM base contains the voltage divider for the PMs working with grounded cathode to allow grounding of the tube shieldings and an A.C. coupled preamp which drives the cables carrying the signals outside of the magnet yoke. The signals enter three way splitters, providing input to a constant fraction discriminator, a driver for amplitude measurements and first level analog sums for trigger generation. All these functions are mounted on a 9U VME card, containing 30 complete channels. Signals from this card go to the KLOE designed 12 bit ADC's, 2 V×10 ns full scale, and 12 bit TDC's, 25 ps per count.[21] A description of KLOE electronics can be found in ref. 21.

Module Ø was exposed to a test beam at PSI this past July. Analysis of the collected data is underway at present, preliminary results indicate that $\sigma_E/E \sim 5\%/\sqrt{E\ (\mathrm{GeV})}$ and $\sigma_T \sim 66\mathrm{ps}/\sqrt{E\ (\mathrm{GeV})}$. These results are precisely the expected resolutions taking into account the length of the full module (4.3 m) and the reduced quantum efficiency of the mesh PM's, halving the number of photoelectrons.

In sum, we have studied extensively the performance of both the *barrel* and *end-cap* prototypes of the KLOE calorimeter and confirmed the findings with module Ø. Aside from the measured energy and time resolutions quoted, we found the energy resolution to be independent of the incidence angle and we expect very little dependence of the time resolution on incidence. We have verified that the calorimeter can provide some added means to identify pions and muons. Finally, the KLOE electronics performed extremely well at the PSI test, fully to specifications and with very low noise. Therefore, we have succeeded in the design of a calorimeter which satisfy, with some safety margins the requirements of the KLOE experiment.

5.4 Calorimeter Performance

Table 7. Calorimeter Performance.

δ(Shower Apex)	=1 cm
$\delta E/E$	$= 5\%/\sqrt{E\ (\mathrm{GeV})}$
δt	$= 66\ \mathrm{ps}/\sqrt{E\ (\mathrm{GeV})}$

6. CENTRAL TRACKING CHAMBER

6.1 INTRODUCTION

The design of the large tracking chamber for the KLOE detector is driven for the most part by the following considerations:

1. Maximize the homogeneity and isotropy of the active tracking volume because of the long decay path of the K_L and the isotropic angular distribution of the charged decay products.
2. Achieve a high and a well controlled efficiency for the reconstruction of $K_L \to \pi^+\pi^-$ decays.
3. Maximize, without forgetting the points above, the fiducial volume for decay detection, to obtain the largest event sample for a given delivered luminosity.
4. Optimize resolution at low momentum values.
5. Minimize the number of wires, both sense and field, in order to ease the difficulties of building a transparent chamber shell, minimize multiple scattering and maintain the electronics channels count within reasonable limits.

The decay length of K_L's, λ_D=350 cm, requires that a long decay path be available to observe a significant fraction of their decays. A reasonable compromise is to detect K_L decays in a big, cylindrical chamber of radius $\sim$ 2 m and length 370 cm. The above tracking volume is located inside a 15 X_0 thick, lead-scintillating fiber e.m.calorimeter, surronded in turn by a superconducting coil providing and a solenoidal field of 0.6 T. The mechanical structure of the drift chamber, with spherical end plates, can withstand without deformation the tension of some 50,000 wires with good transparency ($\leq 0.1X_0$) to photons from π^0 decays, to be detected in the calorimeter.

The uniform distribution of K_L decay vertices and secondary tracks in the chamber volume requires a constant size drift cell. This is achieved by using only alternating stereo layers, with constant inward radial displacement at the chamber center. This results in a stereo angle which increases with radius, 50 mrad $\leq \theta_{st} \leq$ 120 mrad, and an approximately constant, square cell shape along z, with constant wire gain.

Because of the low momenta of the decay products, <300 MeV, we have tested helium-based gas mixture to minimize multiple scattering. A satisfactory choice is a 90-10 mixture of He-iC_4H_{10} whose radiation length is X_0=1300 m. The wires, W for sense and Al for field, result in a final value X_0=900 m. The choice of a relatively big drift cell of 3 $\times$ 3 cm^2 helps in reducing the total amount of material in the chamber, while still maintaining a proper time-space correlation over most of the cell. Drift velocity is generally not saturated. For an expected resolution on any single measurement of $\sigma_{r\phi} \leq 200$ μm, the $K_L \to \pi^+\pi^-$ vertex is expected to be reconstructed with accuracies $\sigma_{x,y} \leq 500$ μm, $\sigma_z \leq$1–2 mm. The resolution for the reconstructed K_L mass is $\sigma_M \sim$1 MeV.

The low drift velocity of He gas mixtures, and the smallness of the Lorentz angle, implies that the magnetic field will only change the time-space correlation without loss in either resolution or efficiency.

The mechanical structure has been computed with the standard finite element analysis programs, in various configuration, as well as tested on scaled down structures. Performance of the proposed cell structure has been both simulated and tested in prototypes of various sizes.

6.2 Mechanical Structure

The requirement of the KLOE chamber that all its walls and the preamplifiers mounted on the chamber end plates must have the lowest possible thickness, in order to minimize photon conversions before the electromagnetic calorimeter as well as multiple scattering and energy losses of charged particles entering the chamber dictated a detailed study in their design. While some bending of the end plates can be acceptable,[33] flat plates are unacceptably thick. Thin conical or spherical plates can carry the load of the wires, with deformations of $\mathcal{O}(1\text{ mm})$.[34] The plate deformation under load is strongly helped by properly attaching the plate outer rim to a torsionally stiff ring.

The end plates of the KLOE chamber are kept apart by twelve rods attached to an outer ring. Gas seal is completed by twelve panels which will be mounted after chamber stringing and an inner cylinder. This last is attached to the end plates via two rings at the center of the plates which also provide support for the low β insertion. Panels and inner cylinder carry no loads in our chamber design, see figure 20.

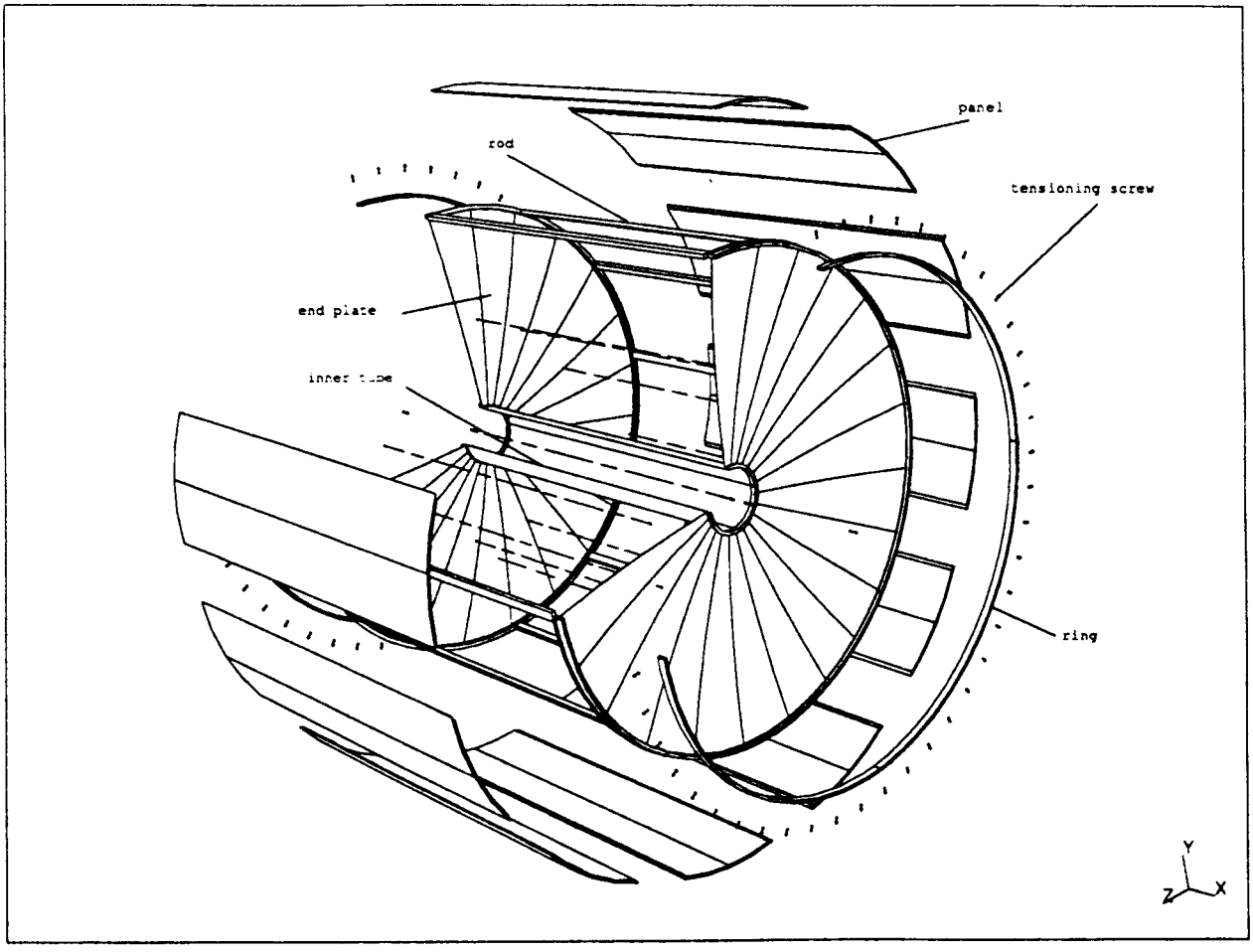

Fig. 20. Exploded View of the KLOE Chamber.

A static analysis of the chamber structure has been carried out with the finite element computer code Ansys 4.4A in order to determine deformations and stresses. The axial deformations of dome and cone shaped, carbon-fiber end plates have maximum displacements which are sim-

ilar, 2.2 and 1.7 mm for conical and spherical shapes respectively, with a smoother behaviour in the latter case. The dome shape might be harder to manufacture. Similar results are obtained for aluminum. We also sudied the deformation of a cone whose outer rim is ideally constrained. In all cases deformations and stresses are well below the elastic limits of the materials.

6.3 CELL SIZE CHOICES

The chamber optimization work is largely based on extensive Monte Carlo simulation work and results obtained with small prototypes exposed to a pion beam at the Paul Scherrer Institüt, Villigen, Switzerland. The simulation results are given in detail in chapter 9 of ref. 20. Such studies show that the single track losses are smaller for a 2×2 cm^2 cell, that the overall loss for full $K_L\rightarrow\pi^+\pi^-$ reconstruction increases from 3.1% to 4.6% with a 3×3 cm^2 cell. However, given the large difference in number of wires for the two cases, $(3/2)^2$=2.25, we feel that the larger cell is an acceptable compromise.

The complete analysis of the test beam data can be found in appendices 3, 4 and 5 of the same reference and results have been presented at conefences.[35] These tests demonstrate that square drift cells do work in a He-based binary gas mixture, with a single cell efficiency > 99% and spatial resolution well within the design specifications of 200 μm. The spatial resolution is not significantly degraded close to the sense wire due to the fluctuations on the number of released clusters, nor far from it due to diffusion. The contribution due to amplification fluctuations is also controlled by the slow drift velocity of the gas mixture. No differences have been observed, neither in efficiency nor in spatial resolution between the 3:1 and 2:1 cell configurations. The space-time relation for the latter is less uniform than for the former, requiring in the end more computer time for track reconstruction. This is of course true only for some special orientations of the tracks and is quite minor on average.

A possible configuration, assuring good tracking also for $K_S\rightarrow\pi^+\pi^-$ decays, might consist of twelve layers in the inner part of the chamber with 1.5×1.5 cm^2 cells, followed by 3×3 cells. The number of cell layers for this case is 61 for a total number of cells of ~13,000. This choice is not too far from an optimal configuration.

6.4 TEST IN MAGNETIC FIELD

A drift chamber prototype consisting of a matrix of 7×7 square cells with sides of 3 cm, operated in a 90%He$-$10%iC_4H_{10} gas mixture, was tested in a 50 GeV/c particle beam at the CERN SPS.[36] A system of aluminum tubes operated in streamer mode provided an external tracking system while the trigger for the passage of a particle was given by the coincidence of two scintillator counters upstream and downstream of the prototype. The counters also provided the reference time t_0 for the drift time measurements in the tracking detectors. The prototype was located inside a magnet, which could produce a field of 0.6 T, with orientation parallel to the wires.

The space-time relation, and therefore the electron drift velocity, is measured using the time measurements from the prototype itself and the track impact point interpolated from the external tracking system measurements. Since the drift velocity in He gas mixtures is not saturated, the fit involves at least a second order polynomial. The measured drift velocity is

in the range of 25 μm/ns. The spatial resolution can be measured in several ways, to a certain extent independent from each other:

1. comparing the drift distance obtained inverting the space-time relation to the track reconstructed using the external tracking system only, or the prototype chamber itself, or both;

2. measuring the resolution with which measurements in nearby cells correctly reproduce the distance between the wires, projected onto the direction of the incoming track. All these methods consistently give a spatial resolution of $\simeq$ 120 μm.

The effect of the magnetic field is measured to be small ($\simeq 5 \div 10\%$ change in drift velocity), as expected, given the low value of the Lorentz angle.

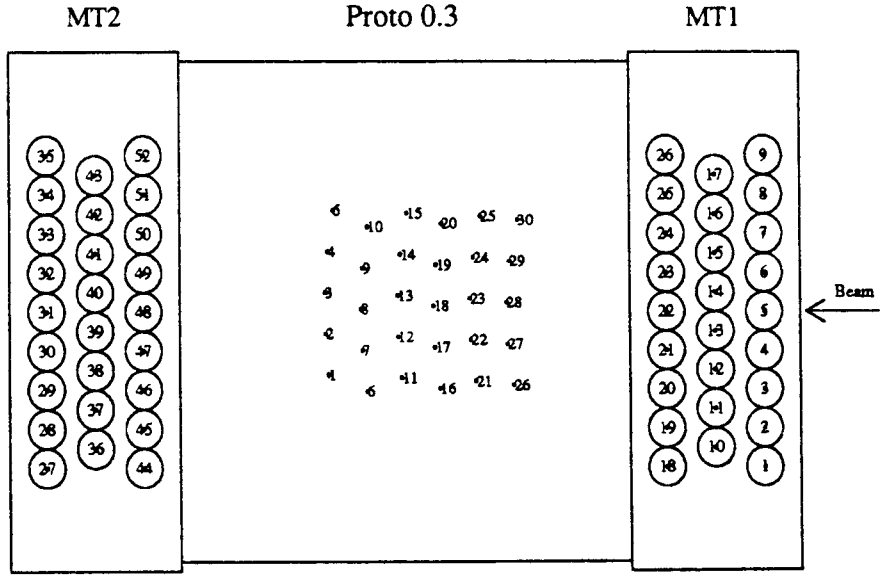

Fig. 21. Set-up of the two trackers MT1, MT2 and the KLOE test chamber.

6.5 Prototype 1

In order to acquire first hand experience about all problems concerning materials, stringing procedure, gas tightness, signal and HV, etc. we have built a full length prototype. The prototype, built with carbon fiber plates furnished by STESALIT A. G. of Zullwil, Switzerland, is 3.2 m long with 1 m^2 end plates, see figure 22.

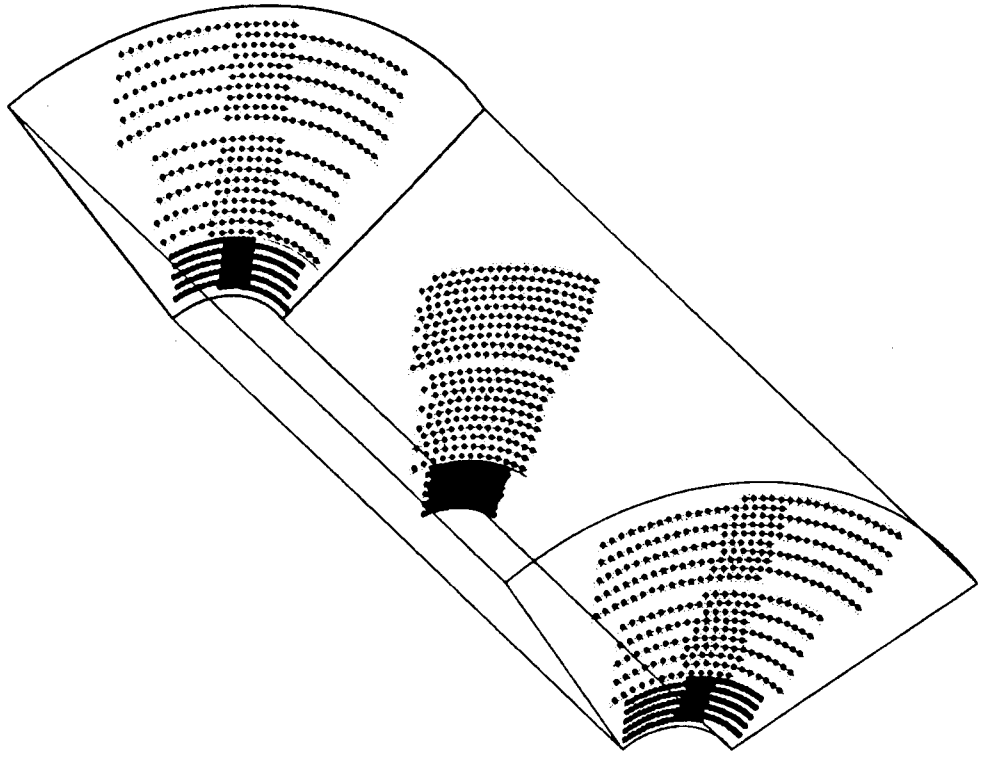

Fig. 22. View of Prototype I showing the position of the wires at the two endplates and at the center.

Five hundred single sense wire square cells, 3cm by 3cm and 1.5cm by 1.5cm, arranged in thirty layers, are strung at stereo angles in the range 50-120 mrad between two conical shaped carbon fiber end-plates. The electron drift occurs in a mixture of helium and isobutane (90/10).[37] Cosmic ray test results confirm that it is invaluable for acquiring experience about all phases of the project.

6.6 Chamber Parameters

The performance required of the KLOE tracking device is given below:

Table 8. Central Chamber Performance.

Drift Chamber,	He gas mix, thin walls
δpoint	$= 200\ \mu$m, r and ϕ
	$= 2$ mm, z
δp_t	$= 0.5\% \times p_t$
$\delta(\tan(\theta))$	$= (3.5 \oplus 2.5) \times 10^{-4}$

7. FRONT-END ELECTRONICS

7.1 Overview

The KLOE detector contains 5,000 photomultipliers, PMs, for the readout of the calorimeter, and ~13,000 wires for the tracking chamber. The PM signals are amplified in the PMs' bases and sent to analog boards of 30 channels each. The outputs of this board are connected to ADCs, TDCs and to the trigger processor. The chamber signals are preamplified at the wire feed-through and sent to boards of 48 channels each. The output of two of these boards are connected to a 96 channel TDC board for drift time measurements.

7.2 Calorimeter Front End Electronics

The calorimeter front end electronics consists of the following functional elements:

1. High voltage divider for the photomultiplier tubes, PMs, which are operated with grounded cathode and positive voltage on the anode, to avoid noise related to charging of surfaces in contact with the tube envelopes.
2. A.C. coupled preamp, for optimal coupling to the PM and driving the cable carrying the signals to the following stage.
3. A three way splitter of the analog signal to provide inputs to:
   (a) Fast, low slew, constant fraction discriminators, for time measurements with the KLOE TDCs;
   (b) Drivers, for amplitude measurements with the KLOE ADCs;
   (c) First level adders for the preparation of the signals for the KLOE trigger.

Voltage dividers and preamplifiers are built as small hybrid assemblies, mounted on the PM socket and located therefore inside the KLOE detector. Signals from the preamps are carried outside the KLOE iron yoke to the rest of the electronics via miniature coaxial cables. The preamplifier is a three transistor transimpedence device, with a conversion gain of 500 V/A. The amplifier output is connected to the cable with a series resistor equal to the impedence Z of the cable and a capacitor. The cable is also terminated at the receiving end. The back termination at the transmitting end insures negligible reflections from imperfect cable termination. It also provides a large effective time constant for the required AC coupling without the use of large capacitors.

The above elements a), b) and c) reside in 9U VME cards. Each card carries 30 channels of this electronics (dictated by the calorimeter structure which consists of 5 sections in depth) plus an as yet undefined number of adders. The signal splitting function is provided by two emitter followers and an amplifier identical to the PM preamp, operated as a unity gain voltage amplifier. Emitter followers are adequate for driving the fast discriminators and the adders for which linearities of 1-2% are quite acceptable, while a precision amplifier insures much better linearity for amplitude measurement and provides a good drive for the cable carrying the signal to the ADC boards.

The fast, low slew, constant fraction discriminator uses the standard technique of subtracting a delayed, inverted replica of the PM signal from the input signal, producing a bipolar signal. A fast, high gain comparator detects the zero crossing time, thus providing partial compensation

of the variation in response time of the comparator with signal amplitude. Prototypes give time walks of 200 ps for input signals of 20 to 1,500 mV. The output of the discriminator is complementary ECL, and is carried to the TDC boards with twisted pairs.

The adders, are fast, linear transimpedence amplifiers using the same design as the PM preamps. At present, 6 five input adders on a card provide a signal proportional to the energy deposition in a basic calorimeter segment. The proposed solution for the high voltage system is based on commercial components from CAEN.

The KLOE calorimeter signal processing poses some special problems because the signal to be measured can appear over an interval $\Delta t \sim \pm 100$ ns with respect to the trigger signal. We use a modified double sampling technique, following the integration of the PM signals. The integrated signal baseline is continuously sampled at fixed frequency on two capacitors and is also sampled again some time after the trigger on a third capacitor. The difference of this last sample with the correct baseline sample, obtained in analog, is the integral of the PM signal and is digitized by a 12 bit, 1 μs commercial ADC. The 30 channel board will be 9U high and 400 mm deep, with a standard VME interface and a fast custom readout bus that uses the free row of the P2 connector. The main functions implemented on the board, for data processing and readout, are: offset subtraction, empty channel suppression in order to reduce the amount of data read out and multi-event buffering to allow asynchronous readout.

The measurement of the time-of-arrival at the electromagnetic calorimeter is performed in a common start mode, the start being provided by the main trigger signal, synchronized with the bunch crossing time. Each TDC channel is built around a monolithic time-to-amplitude converter developed in bipolar technology, followed by a 1 μs conversion time 12 bit monolithic ADC chip. Each calorimeter signal is delayed by 100-300 ns with a monostable circuit and used as a stop. 30 TDC channels reside on a VME card. Full scale of a channel is 100 (200) ns with a resolution of 25 (50) psec and an integral non linearity of $\sim$0.1%. Functions implemented on the board for data processing and readout are: empty channel detection/suppression via table look-up, hardware offset subtraction, via table look-up and multi event buffering to allow asynchronous readout.

Module Ø tested to great satisfaction the following chain of the final KLOE electronics at PSI in June 1994: PM bases containing the voltage divider and an A.C. coupled preamp which drives the cables carrying the signals to the outside, splitters which provide input to a constant fraction discriminator and to a driver for amplitude measurements, the KLOE designed 12 bit ADC's and 12 bit TDC's.

7.3 Front End Electronics for the Drift Chamber

It is common practice to amplify the sense wire signals at the place where they first become available, the wire feed-throughs. An investigation of different preamplifiers[38] has shown that the VTX chip[39] is the best one thanks to its extremely low power dissipation, package mass and price/channel. Specifications for this preamplifier are listed in table 9.

Table 9. Preamplifier specifications

Gain	1.0 mV/fC (50 Ω load)
Dynamic range	400 mV (3% linearity at max output)
Crosstalk	<0.5% between any two channels
Noise	860 electrons + 47 e/pF, 100 MHz bandwidth
Output risetime	5 nS
Output falltime	16 nS
Input impedence	130 Ω
Output impedence	43 Ω
Power dissipation	10m W/channel, 1 mA output pulldown current
Channels/chip	6

Since the VTX is provided as a bare die with six channels it is mounted on a card with the ancillary components. Sense wires are coupled through a 470 pF, 3 kV capacitor. Each preamplifier is protected against high voltage sparking by a diode pair and two resistors chosen to provide a series termination for the sense wire when added to the input impedence of the preamplifier. A calibration input is provided for calibration and test purposes.

Signals from the wire preamplifiers will be brought out of the KLOE detector by means of miniature 50 ohm coaxial cables. Because the expected signals from single electron clusters have an amplitude of about 10 mV, they need to be amplified before discrimination. An analog signal is also provided for pulse height measurements. The first stage is a $\times 10$ amplifier with low input impedance for transmission line termination. This stage drives both the analog output buffer and the comparator driving stage. The total voltage gain at the input of comparator is $\sim$ 25. The comparator produces a differential ECL pulse whose minimum width is fixed to 100 ns. The threshold is adjustable through a 10 to 1 voltage divider. An input is also furnished for calibration/test purposes. Specifications for the amplifier-discriminator circuit are given in table 10.

Table 10. Amplifier and discriminator circuit specifications

Analog output voltage gain	5
Voltage gain (comparator input)	$\sim$ 25
Output risetime	$\sim$ 5 nS
Dynamic range (analog output)	$\sim$ 1.5V
Analog output	unipolar, 50 Ω
Digital out	diff. ECL, $\sim$ 110 Ω
Calibration Input	one per card

Forty-eight amplifier-discriminator channels are packaged on a single VME 9U card together with circuits for threshold setting/sensing and the logic for addressing. Thresholds can be set for groups of 8 channels. An additional card in each crate of amplifier-discriminators is used for communication with the slow-control devices for threshold sensing/setting and calibration/test

signal generation. Communication between the slow-control processor and the crates is via an RS232 serial link. The calibration circuit is used to supply calibration signals to the preamplifiers. A DAC controls the charge injected into the preamplifiers. Fixed amplitude signals for testing the amplifier-discriminators are also generated by this card.

7.3.1 High Voltage System

The requirements for the HV system are:

1. programmable voltage setting (0 - 2.5 kV, 1V resolution, master);
2. programmable hardware trip (50 nA - 1 μA, distributor);
3. programmable ramp down (master);
4. programmable ramp up (master);
5. voltage sensing (1 V resolution, distributor);
6. single channel on/off capability (distributor).

Each HV channel supplies a group of sense wires connected by a daisy chain (we expect to use a modularity of 6/12 wires per HV channel).

7.3.2 Chamber TDCs

The TDC chips for the KLOE chamber digitization will reside in groups of three (96 channels) on modules fitting into the KLOE custom crates and readout scheme. Most of the functionality, digitization and event buffering, is integrated into a VLSI chips. The measurement of the signal drift-time coming from the chamber is performed by a custom integrated circuit, which is under development by the INFN Sezione di Roma1. The circuit is a multichannel common start/stop TDC, with 32 channels per chip. In KLOE the drift-time measurement is done by recording, for each signal, its time of arrival with respect to a stop signal, which is common to all channels and generated by the trigger. The TDC integrated circuit will be developed as a full-custom device in 0.5 micron CMOS technology. Its working frequency is a function of an external reference clock that must be supplied to the circuit and it can be as high as 1 GHz (1 nsec LSB). The circuit is capable of detecting rising/falling edges, with a double edge resolution of 10 nsec or better. A programmable number of hits, from 1 to 16, can be stored for each channel. The hits are recorded as 16 bit words and every registered hit is stored in the chip for a programmable time interval. If during this time the chip does not receive a stop command the hit is removed, otherwise, the hit is kept for the read-out. The chip has also a multi event buffering capability, 4 events deep, which is used only if at least one hit is present in one of the 32 channels, in a time window associated with a stop signal. Dedicated prompt trigger output lines inform the read-out of the presence in the chip of data to be read. The read-out of the data passes through the I/O port at a maximum speed of 50 MHz. The empty channels are automatically skipped during the read-out phase and for each registered hit the chip gives its absolute time value with respect to the stop signal and its channel number. Additional chip functions include an event counter; masking of the individual channels; and a self-test facility. Three of these chips will be mounted on a 9U VME board, for a total of 96 channels.

8. DATA ACQUISITION

8.1 Introduction

The major aim of the KLOE experiment at DAΦNE (Frascati) is to perform CP violation studies at sensitivities of $\mathcal{O}(10^{-4})$. The KLOE data output of $\mathcal{O}(10^{11}$ events/year) must therefore be handled by its data acquisition system, DAQ, maintaining biases to values smaller than the experimental accuracy sought. The maximum expected data rate from the KLOE detector, at full DAΦNE luminosity, has been estimated as 10^4 events per second of 5 kbytes each in average, corresponding to a total bandwidth of 50 Mbytes/s. The major components of the KLOE DAQ system are briefly presented in the following.[40] An overall view is given in fig. 23.

8.2 Architecture

Data comes from ~25,000 Front End Electronics, channels housed in some 40 9U-VME crates. Signal conditioning and digitization is performed in a fixed time of $\mathcal{O}(2\ \mu s)$, to avoid biases depending on event configuration. Every FEE channel contains buffers of appropriate depth, in order to eliminate data overflows and to allow asynchronous read-out.

8.2.1 Fast Data Read Out

Data from the FEE are transferred to an on-line farm of Single Board Computers, SBC, using a two level concentration scheme. The first one is performed at crate level via a custom bus in the backplane, the AUXbus, and a hardwired read-out controller, ROCK, located in the crate itself. The ROCK implements the function of a sparse readout scanner collecting data related to each single trigger. The second level of concentration is performed by a ROCK manager, ROCKM, connected to chains of crates of suitable length with a cable bus, Cbus. Each ROCKM resides in a 6U-VME crate together with a VME processor which prepares sub-events for transmission to a given farm element. A commercial VME interconnector, VIC, connects all the crates in a chain allowing VME processors to program, check and debug FEE, ROCK's etc.

The components of the DAQ system are interconnected via Ethernet for low bandwidth operations (controls, downloading, monitoring) and via FDDI for data transmission. A DEC FDDI GIGAswitch, with bridge functionality, is used to provide parallel paths between the VME processors and the farm in a scalable way. The number of switch ports dedicated to chains is chosen taking into account two factors: the maximum acceptable read-out ROCKM time and the throughput of the communication protocol achievable at VME and farm level. In order to improve the performance of the communication protocol, the sub-events related to the same group of consecutive trigger numbers are packed in sub-event-strings that must be gathered by a single SBC.

8.2.2 Data Flow Control and Event Building

The farm SBC's build and test the integrity of each event, implement the final event formatting, and perform quality control on samples of the data. The address of each farm element is assigned by an additional VME processor, the data flow controller, DFC, connected also via VIC channels to the ROCKM crates. The DFC manages the load of all the VME processors, maintaining a table which maps groups of trigger numbers and SBC addresses. DAQ resets and

buffer flush-out commands are generated when misalignment is detected at farm level. Other error conditions will be similarly handled.

The farm is based on SBC's organized in crates. Each crate has a dedicated output SBC which manages the crate I/O to the storage devices. The total CPU power required for the whole farm is estimated to be about 16,000 Specint'92. CPU boards adequate for this are beginning to appear in the market. We wait for a final decision upon the outcome of a joint project between INFN and DEC designing a custom SBC using the DEC Alpha chip.

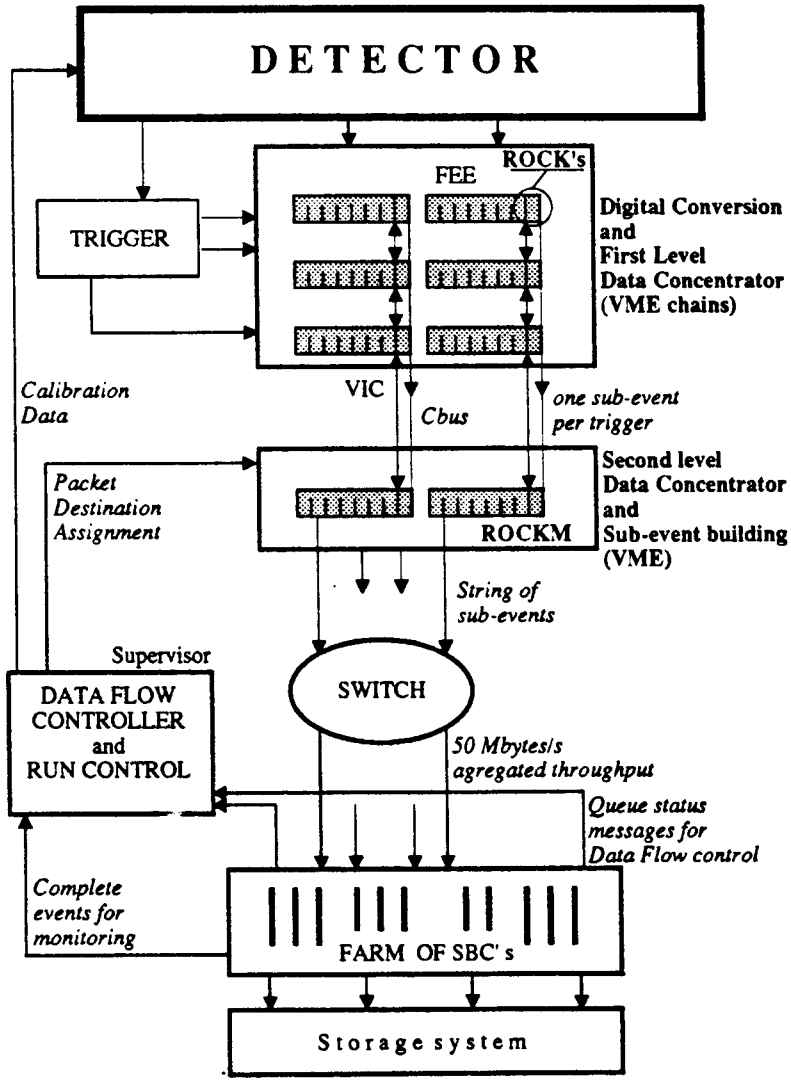

Fig. 23. System Architecture and Information Flow.

8.3 Software and Storage

The on-line software represents a challenge because beyond the first level of data concentrators, the software must maintain the event synchronization. In a 10 kHz rate DAQ system, the latency time for message transmission is most important. In 1 ms, there are 10 events accumu-

lating in the buffer queues. Message losses and consequent retransmissions have to be considered as failures. The general software architecture is based on UNIX concepts implemented on non-homogeneous hardware platforms. Real-time operating system will run in each board where diskless operation is needed. TCP/IP is used as underlaying transport protocol for data transmission and message passing, while SNMP is used for network monitoring. Furthermore, DFC uses SNMP to build its tables.

The amount of data collected in a year of running is of the order of 500 Tbytes. While the on-line system requires only tape loaders, the off-line analyses require a compatible robotic system able to manage this huge quantity of data. A database is needed, which will contain all relevant information regarding the runs and the events, such as calibration constants, trigger condition, detector configuration, collider status and performance, fill numbers, run numbers, etc. Part of this information comes also from the on-line farm in dedicated banks such as the Run Header or the Event Header, to simplify trace back and raw data tape searches. No "event directory" is used for the raw KLOE data, but the chosen database will assure the compatibility with the file system used in the tape robots. The most promising tape system, in terms of performance/cost, appears to be the DEC DLTs.

ACKNOWLEDGEMENTS

I wish to thank Gaetano Vignola for the informations on DAΦNE, to acknowledge and thank all my KLOE colleagues for their wonderful and heroic efforts to realize KLOE. I also wish to thank Paula J. Franzini and Paolo Franzini for help in preparing this paper.

REFERENCES

1. G. Vignola, *Proc. of the Workshop on Physics and Detectors for DAΦNE*, G. Pancheri Ed., Frascati, 1991, p. 1.; G. Vignola, Proceedings of the XXVI International Conference on High Energy Physics, Dallas, 1992. ed. J. R. Sanford, 1941, AIP Conf. Proc. No. 272 (1993).
2. Review of Particle Properties, Particle Data Group, Phys. Rev **D50**, 1173 (1994).
3. KLOE, A General Purpose Detector for DAΦNE, the KLOE Collaboration, Preprint LNF-92/019, April 1, 1992; "KLOE, A General Purpose Detector for DAΦNE" (P. Franzini), with the KLOE Collaboration, Proceedings of the XXVI International Conference on High Energy Physics, Dallas, 1992. ed. J. R. Sanford, 1885, AIP Conf. Proc. No. 272 (1993).
4. "THE KLOE DETECTOR, *Technical Proposal.*"the KLOE Collaboration, LNF-93/002 (IR), January 1993.
5. C. D. Buchanan *et al.*, Phys. Rev. **D45**, 4088 (1992).
6. L. Maiani, *The DAΦNE Physics Handbook*, L. Maiani *et al.* Eds., Frascati, 1992, V. I, p. 21.
7. For all references on CHPT, see *DAΦNE Physics Handbook*, ed. L. Maiani *et al.*, LNF, Frascati.
8. M. Bailargeon and P. J. Franzini, PSI-PR-94-25, 1994.
9. F. E. Close, the *The DAΦNE Physics Handbook*, 465, 1992.
10. J. Lee-Franzini, W. Kim, and P. J. Franzini, *The DAΦNE Physics Handbook* p. 533.
11. N. Brown and F. Close, *The DAΦNE Physics Handbook* p. 447.
12. J. Lee-Franzini, W. Kim, and P. J. Franzini, Phys. Lett. **B287** 259 (1992); *The DAΦNE Physics Handbook* p. 513.
13. A. Bramon, G. Colangelo, P.J. Franzini and M. Greco, *The DAΦNE Physics Handbook* p. 487.

14. P. J. Franzini and G. Colangelo, Phys. Lett.**B289**, 189 (1992).
15. W. Kluge, Proc. of the *Workshop on Physics and Detectors for DAΦNE*, Frascati, 1991, p. 469; W. Kluge, KLOE Note no. 15, Dec. 91.
16. T. Kinoshita, B. Nižić and Y. Okamoto, Phys. Rev. D **31**, 2108 (1985), and references therein; see in particular their reference 28.
17. R. Jackiw and S. Weinberg, Phys. Rev D **5**, 2396 (1972); G Altarelli, N. Cabibbo and L. Maiani, Phys. Lett. **40B**, 415 (1972); I. Bars and M. Yoshimura, Phys. Rev. D, **6**, 373 (1972); W. A. Bardeen, R. Gastmans and B. E. Lartrup, Nucl. Phys. **B46**, 319 (1972).
18. P. Franzini, *'89 Electroweak Interactions and Unified Theories, XXIV Rencontre de Moriond*, J. Tran Than Van Ed., Edition Frontière, Gif-sur-Yvette, 1989.
19. S. Bartalucci *et al.*, Nuovo Cimento, **49A**, 207 (1979).
20. *The KLOE Central Drift Chamber*, the KLOE Collaboration, LNF Report LNF-94/028, 1994.
21. *The KLOE Data Acquisition System*, the KLOE Collaboration, LNF Report LNF-94, 1994.
22. J. H. Christenson *et al.*, Phys. Rev. Lett. **13**, 138 (1964).
23. Geanfi is the general purpose KLOE's Monte Carlo program based on the CERN GEANT code. See A. Antonelli, C. Bloise and A. Calcaterra, KLOE note 3, 1991
24. G. de Zorzi, *Proc. of 4th Int. Conf. on Calorimetry*, La Biodola, Italy (1993).
25. H. Hinterberger, R. Winston, Rev. Sci. Instr. 37 (1966) 1094; A. Di Domenico *et al.*, KLOE Notes 83 and 84.
26. S. Miscetti, *Proc. of 4th Int. Conf. on Calorimetry*, La Biodola, Italy (1993).
27. J. Lee-Franzini, *Proc. of 6th Int. Conf. on Advanced Detectors*, Elba, PISA, Italy (1994).
28. D. Babusci *et al.*, Nucl. Instr. and Meth. 305 (1991) 19.
29. S. Miscetti and A. Parri, KLOE note 111 (1994).
30. C. Bini *et al.*, KLOE Notes 42, 50, 60, and 78; G. Barbiellini *et al.*, KLOE Notes 56 and 81.
31. F. Bossi, KLOE notes 54 and 91.
32. L. Keeble, G. Lanfranchi and M. Anelli, KLOE Notes 90, 96 and 109.
33. D.G.Cassel et al., Nucl. Instr. and Meth. **A252**, 325 (1986).
34. R. J. Roark, W. G. Young, Formulas for stress and strain, Mc Graw Hill (1985).
35. G. Finocchiaro, *Proc. of 6th Int. Conf. on Advanced Detectors*, Elba, PISA, Italy (1994).
36. F. Lacava, with the KLOE Chamber Group, Vienna Wire Chamber Conference 1995.
37. F. Grancagnolo, with the KLOE Chamber Group, Vienna Wire Chamber Conference 1995.
38. M. Carletti, G. Felici, P. Locchi, Chamber front-end status report, KLOE note N. 66.
39. R. J. Yarema et al., A High Performance Multi-Channel Preamplifier ASIC, IEEE Transaction on Nucl. Sci., 39 (1992).
40. *THE KLOE DATA ACQUISITION SYSTEM, Addendum to the Technical Proposal*, The KLOE Collaboration, LNF-94 (1994).